Chemical Engineering Journal

Electrochemical Performance of Titanium (Ti), Antimony-Doped Tin Oxide on Titanium (NiATOTi) and Platinum- Antimony-Doped Tin Oxide on Titanium (NiATOTiPt) Anodes in Closed Loop Flow Wastewater Treatment

--Manuscript Draft--

Manuscript Number:	CEJ-D-25-39018R3
Article Type:	Research Paper
Keywords:	Electrochemical oxidation; advanced oxidation process; Hydroxyl radical; methylene blue; Textile Wastewater; DFT
Corresponding Author:	Chedly Tizaoui Swansea University Swansea, UNITED KINGDOM
First Author:	Chedly Tizaoui
Order of Authors:	Chedly Tizaoui
	Navneet M. Yadav
	Sina Younesi
	Ibrahim THOLLEY
	Richard E. Palmer
Abstract:	This study addresses the efficiency of antimony-doped tin oxide (ATO)-based electrodes for electrochemical oxidation. We synthesised and compared three electrodes: bare titanium (Ti), nickel-ATO on Ti (NiATOTi), and platinum-nickel-ATO on Ti (NiATOTiPt), fabricated via metal coating and annealing at 520°C. Comprehensive characterisation using XRD, EDS, SEM, and XPS confirmed phase structure, metal distribution, and composition. Electrochemical performance was assessed using methylene blue dye degradation, ·OH generation, and Electrical Energy per Order (EEO). NiATOTiPt exhibited the highest ·OH production and the lowest EEO, attributed to enhanced charge transfer and homogeneous surface properties. At 5V, its degradation rate constant was 2.6 and 1.3 times higher than NiATOTi and Ti, respectively, increasing to 7.5 and 3.3 times at 10V. A strong linear correlation was observed between degradation rate and ·OH generation. While higher circulation flow rates improved degradation, excessive flow led to channelling, reducing efficiency. Ozone formation was negligible, confirming ·OH as the main oxidant. Repeated use of NiATOTiPt electrode did not significantly affect its performance, showing higher degradation kinetics in simulated textile wastewater than in deionised water, albeit with higher EEO. Degradation products were identified and monitored using LC-MS/MS, and a degradation mechanism was proposed based on density functional theory (DFT) calculations. Fukui f0 values correlated strongly with rate constants (R2=0.991), indicating that higher local f0 leads to faster degradation. Overall, NiATOTiPt demonstrated superior efficiency, achieving EEO values below 1kWh/(m3.order) for solutions in DI water and below 10 kWh/(m3.order) for simulated textile wastewater. These findings suggest that ATO-based electrodes, particularly NiATOTiPt, hold strong potential as an advanced oxidation process for effective and energy-efficient water treatment.

Graphical Abstract

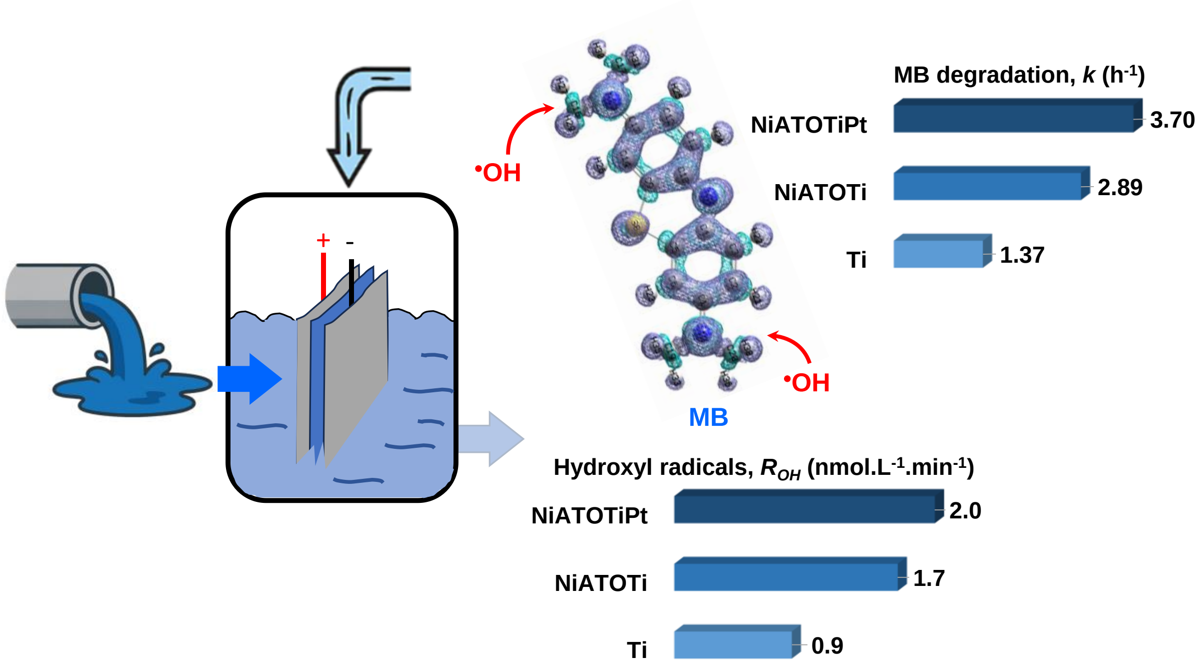

Highlights

- NiATOTiPt showed the highest hydroxyl radical production and lowest energy use.
- Strong linear correlation found between degradation rate and $^{\bullet}$OH production.
- ATO-based electrodes achieved EEO below 1 kWh/m^3.order for dye removal.
- Flow rate impacted mass transfer efficiency and overall degradation performance.
- LC-MS/MS and DFT revealed MB degradation pathway and intermediates.

Electrochemical Performance of Titanium (Ti), Antimony-Doped Tin Oxide on Titanium (NiATOTi) and Platinum- Antimony-Doped Tin Oxide on Titanium (NiATOTiPt) Anodes in Closed Loop Flow Wastewater Treatment

Navneet Yadav[1,2], Sina Younesi[1], Ibrahim Prince Tholley[1], Richard E. Palmer[2], and Chedly Tizaoui[1*]

[1] Water and Resources Recovery Research Lab, Department of Chemical Engineering, Swansea University, Bay Campus, Fabian Way, Swansea SA1 8EN, UK

[2] Nanomaterials Lab, Department of Mechanical Engineering, Swansea University, Bay Campus, Fabian Way, Swansea SA1 8EN, UK

Correspondence: E-mail: C.Tizaoui@swansea.ac.uk

Abstract

This study addresses the efficiency of antimony-doped tin oxide (ATO)-based electrodes for electrochemical oxidation. We synthesised and compared three electrodes: bare titanium (Ti), nickel-ATO on Ti (NiATOTi), and platinum-nickel-ATO on Ti (NiATOTiPt), fabricated via metal coating and annealing at 520 °C. Comprehensive characterisation using XRD, EDS, SEM, and XPS confirmed phase structure, metal distribution, and composition. Electrochemical performance was assessed using methylene blue dye degradation, $^{\bullet}$OH generation, and Electrical Energy per Order (EEO). NiATOTiPt exhibited the highest $^{\bullet}$OH production and the lowest EEO, attributed to enhanced charge transfer and homogeneous surface properties. At 5 V, its degradation rate constant was 2.6 and 1.3 times higher than NiATOTi and Ti, respectively, increasing to 7.5 and 3.3 times at 10 V. A strong linear correlation was observed between degradation rate and $^{\bullet}$OH generation. While higher circulation flow rates improved degradation, excessive flow led to channelling, reducing efficiency. Ozone formation was negligible, confirming $^{\bullet}$OH as the main oxidant. Repeated use of NiATOTiPt electrode did not significantly affect its performance, showing higher degradation kinetics in simulated textile wastewater than in deionised water, albeit with higher EEO. Degradation products were identified and monitored using LC-MS/MS, and a degradation mechanism was proposed based on density functional theory (DFT) calculations. Fukui f^0 values correlated strongly with rate constants (R^2=0.991), indicating that higher local f^0 leads to faster degradation. Overall, NiATOTiPt demonstrated superior efficiency, achieving EEO values below 1 kWh/(m^3.order) for solutions in DI water and below 10 kWh/(m^3.order) for simulated textile wastewater. These findings suggest that ATO-based electrodes, particularly NiATOTiPt, hold strong potential as an advanced oxidation process for effective and energy-efficient water treatment.

Keywords: Electrochemical oxidation; Advanced oxidation process; Hydroxyl radical; Methylene Blue; Textile wastewater; DFT.

1 Introduction

The rapid expansion of industrial activity has resulted in the release of harmful organic pollutants, significantly impacting global environmental quality and human health. These pollutants are key contributors to the contamination of both surface and ground waters [1-3]. The 2024 United Nations World Water Development Report reveals that textile mills are responsible for one-fifth of global industrial water pollution, with textile dyeing the second largest contributor to water pollution worldwide [4]. Specifically, the textile industry discharges wastewaters containing highly toxic, non-biodegradable synthetic dyes into the environment [4-6]. These dyes are known potential carcinogens, and even in trace amounts they pose significant risks to both human health and the environment [7]. For instance, the release of dyes in the aquatic environment can colour the water, reducing light penetration and hampering photosynthesis [8]. Textile dyes are also toxic to aquatic organisms such as fish and invertebrates, interfering with their physiological processes, and causing mutations, inhibited growth or even death. In addition, dyes can cause oxygen depletion in the aquatic environment and negatively impact water quality in rivers, lakes and oceans, reducing the availability of drinking water sources. Thus, the release of textile dyes into the environment not only threatens ecosystems but also hampers progress toward achieving the United Nations Sustainable Development Goal 6 (SDG6), aiming to ensure the sustainable management of water and sanitation for all. Addressing industrial pollution, such as textile dyes, is not only one of the pillars of SDG6 but it is essential for safeguarding both public health and the planet’s water resources. Aligned with SDG6, the Electrochemical Advanced Oxidation Process (EAOP) offers a cleaner and more sustainable method for treating wastewater and removing pollutants, thereby improving water quality by reducing pollution. Besides, EAOP offers multiple advantages over other methods, including low cost, high efficiency, modularity, enhanced process safety, and minimal waste generation [9-12]. As a result, there is increasing interest in using this approach for the effective treatment of wastewater contaminated with organic compounds such as textile dyes. In this study, methylene blue (MB), a synthetic dye with documented toxicity to aquatic organisms and potential health risks to humans at high concentrations [13-15], was selected as a model textile dye. MB is a cationic thiazine dye structurally similar to many industrial dyes used in the textile and printing sectors, containing aromatic rings, heteroatoms, and chromophores such as –C=N– and –S=. These structural features make its degradation behaviour representative of how actual industrial dyes respond to electrochemical treatment. Owing to its environmental relevance, well-characterised chemical structure, and distinctive optical properties, MB serves as an excellent model compound for electrochemical oxidation studies. Its extensive prior use in research also enables direct comparison with literature data and facilitates benchmarking of new electrode materials and treatment technologies.

EAOP utilises electrodes connected to an electrical power supply to generate reactive species, including hydroxyl radicals, hydrogen peroxide, and ozone, to degrade a wide range of contaminants [11, 16-18]. It is particularly effective against organic pollutants, which are often resistant to conventional treatment methods, such as pharmaceuticals, textile dyes, and endocrine disrupting chemicals. A key component of the electrochemical oxidation reactor is the anode, the electrode connected to the positive pole of the power supply, where the degradation of contaminants takes place. Degradation at the anode can occur through direct anodic oxidation, which involves the direct transfer of electrons to the anode and typically results in poor decontamination, or via indirect reactions involving reactive species including physisorbed hydroxyl radicals ($^{\bullet}OH$) or chemisorbed active oxygen [11]. Hydroxyl radicals are the most potent and are key species in EAOP responsible for breaking down the contaminants in water. Their strength of interaction with the anode, which is influenced by the material type of the anode, plays a key role in the overall reactivity of the EAOP process in degrading pollutants. Anodes with high overpotentials for the oxygen evolution reaction (OER) (i.e., poor electrocatalytic ability for OER) are particularly suited for wastewater treatment. The high OER overpotentials of these anodes reduce competition between OER and the oxidation of organic contaminants, thereby enhancing treatment efficiency. Based on the type of hydroxyl radicals formed on the anode surface, anodes in electrooxidation processes are classified as “active” or “non-active” [16, 19]. Active anodes (e.g., Pt, IrO_2, RuO_2) have low OER potential and offer only little partial and selective oxidation of contaminants, while non-active anodes (e.g., BDD, PbO_2, SnO_2-Sb) exhibit high OER potential, resulting in the complete oxidation of organic compounds to carbon dioxide, water, and mineral salts [12, 20]. Thus, an ideal electrode for EAOP processes in water treatment should have a high OER potential to minimise side reactions, while also exhibit weak adsorption affinity for $^{\bullet}OH$ to enhance the generation of highly reactive hydroxyl radicals freely available for degrading contaminants in water coupled with high current efficiency [12, 21, 22].

Generally, dimensionally stable anodes are made by depositing a thin layer of metal oxide on a suitable base metal, a method that has been proven to be highly effective for organic degradation [23, 24]. Titanium (Ti) is a widely used base material substrate for the fabrication of anodes because of its low price, good corrosion-resistance, and high tensile strength [25]. Although boron-doped diamond (BDD) has proven to be an excellent anode in EAOP, its high cost has driven researchers to explore more affordable alternatives such as PbO_2 catalysts. However, concerns regarding the potential leaching of toxic Pb^{2+} from PbO_2 in water treatment persist, which led to the emergence of antimony-doped tin dioxide (SnO_2-Sb or ATO) as a promising alternative electrode. ATO has received particular attention due to its high oxygen evolution potential, low toxicity, and effectiveness in degrading contaminants, yet there are concerns around its stability [16, 26]. Thus, to improve ATO's stability and lifetime, various electrode preparation methods have been undertaken including application of interlayer [27] or doping with metals [28-30].

Despite efforts to develop high-performance ATO electrodes for EAOP, there remains a lack of comprehensive comparisons and benchmarking regarding efficiency improvements as the electrode transitions from virgin Ti material to stable ATO [30, 31]. A key knowledge gap lies in the lack of a quantitative relationship between electrode composition and the generation of active oxidants, particularly hydroxyl radicals. Efficient hydroxyl radical production is a critical determinant of EAOP performance in degrading organics during wastewater treatment. The influence of co-dopants also warrants attention; for instance, in other electrode systems, the addition of dopants such as Pt has enhanced efficiency of the electrochemical process [32, 33]. Furthermore, comparing energy per order (EEO) across ATO variants is crucial to identify configurations that deliver maximum removal efficiency with minimal energy input. A comprehensive characterisation of transformation products is also necessary to ensure that high-efficiency electrodes not only achieve rapid degradation of the parent compound but also avoid generating persistent or toxic byproducts.

To address existing gaps, this study evaluated different ATO electrodes, comparing their performance and providing valuable insights into their ability to generate hydroxyl radicals and the transformation products formed as the reaction progressed over time. Specifically, ATO electrodes were synthesised using the dip-and-dry method, including Ti/Ni-Sb-SnO_2 (NiATOTi), Ti-Pt/Ni-Sb-SnO_2 (NiATOTiPt), and virgin Ti. These electrodes were characterised and compared for their electrochemical oxidation of the textile dye methylene blue (MB), with performance properties evaluated based on degradation times, rate constants, degradation efficiency, surface composition, and $^{\bullet}OH$ production. Triple quad mass spectrometry (LC-MS/MS) was employed to detect transformation products during MB degradation, and plausible mechanisms for the electrocatalytic oxidation of MB were suggested using both the LC-MS/MS data and molecular DFT calculations.

2 Experimental Methods

2.1 Materials

Titanium metal mesh, Nafion-117 membrane and nickel chloride hexahydrate ($NiCl_2{\cdot}6H_2O$) were purchased from Alfa Aesar. Antimony Chloride ($SbCl_3$), Potassium hexachloroplatinate (K_2PtCl_6) and disodium terephthalic acid (Na_2TPA) ($C_8H_4Na_2O_4$) were procured from Acros Organics. Tin chloride ($SnCl_4{\cdot}5H_2O$) and 2-hydroxy terephthalic acid (OHTPA) ($C_8H_6O_5$) were purchased from Sigma-Aldrich. Methylene blue ($C_{16}H_{18}ClN_3S{\cdot}3H_2O$), isopropanol ($C_3H_7OH$) and oxalic acid ($C_2H_2O_4$) were brought from Thermo Fisher Scientific Inc., UK. A simulated methylene blue synthetic textile wastewater was prepared using a slightly modified formulation adapted from previous studies [34, 35] (Text S1), and its composition is summarised in Table S1. All chemicals were of reagent grade and used without further purification. Deionised water was used throughout for the preparation of all the experimental solutions.

2.2 Fabrication of NiATOTi (Ti/Ni-Sb-SnO_2) and NiATOTiPt (Ti-Pt/Ni-Sb-SnO_2) Electrodes

The fabrication of the electrodes started with the preparation of a nickel in antimony tin oxide solution by dissolving 0.050 g of $NiCl_2.6H_20$, 0.050 g of $SbCl_3$ and 5.0 g of $SnCl_4.5H_2O$ in 50 mL of isopropanol and stirred using a magnetic stirrer. This prepared solution is designated as the NiATO solution. The base material was a titanium metal mesh substrate (size 3×3 inches). The Ti mesh substrate was properly cleaned by boiling in an oxalic acid (10 wt%) for 1 h followed by rinsing with distilled water. The cleaned titanium mesh was used as the virgin Ti electrode or for the preparation of the other two electrodes using the dip-dry method. Briefly, the cleaned Ti mesh was dipped in the prepared NiATO solution and dried in a glove box, then it was placed in a hot air oven at 100 ˚C for 10 min, after which it was calcined in an air furnace at 520 °C for 10 min. This process was repeated 7 to 8 times and finally the mesh was annealed in the furnace at 520 ˚C for 1 hour. At the end of this process, the NiATOTi electrode was obtained. The NiATOTiPt electrode was also prepared following the same protocol, but the starting solution was a NiATO solution with the platinum precursor. For electrical connection, a thin layer of copper (Cu) conductor tape was applied over the edges of the annealed NiATOTi mesh.

2.3 Characterisation Techniques

The physical properties of Ti mesh, NiATOTi and NiATOTiPt electrodes were determined using various characterisation techniques. The X-ray diffraction (XRD) profile of the used electrodes was performed on Bruker D8 Discover X-ray powder diffractometer equipped with Cu Kα radiation $\lambda = 1.5406$ Å over a 2Θ range of 20–90˚. A scanning electron microscope (ZEISS Evo LS 25) equipped with a HD backscattered electron detector (BSD) was used to characterise the top-view morphologies of the resulting electrodes. Elemental analysis (EDS and elemental mapping) was performed using an Oxford Instruments EDS detector with Aztec 6.1 software equipped with the same scanning electron microscope ZEISS Evo LS 25.

The surface chemical states and elemental composition of the solutions on the Ti mesh were investigated using a multipurpose X-ray photoelectron spectrometer (XPS). XPS measurements of the resulting electrodes were performed using an Axis Supra XPS system (Kratos Analytical) equipped with a monochromatic Al-Kα X-ray source (1486.7 eV) and a large area slot mode detector (approximately 300 µm × 800 µm analysis areas). FTIR analysis was performed to detect the functional groups formed on the surface of the mesh. Meshes were placed on the ATR crystal of a Perkin Elemer FTIR spectrometer and spectra were measured between 500 and 4000 cm^{-1}.

2.4 Electrochemical degradation set-up

The electrochemical degradation setup is depicted in Fig. 1. The prepared ATO mesh electrodes were used at the anode (+ve) side while a bare titanium mesh was used as cathode (-ve). Both electrode compartments were separated by Nafion-117 membrane as a proton exchanger. A flow of methylene blue solution was introduced at the anode side and recycled back to the reactor in a closed loop mode, while distilled water was introduced at the cathode side, also in a closed loop configuration.

Figure 1

2.5 Analytical methods

A UV–vis spectrophotometer (Cary 60, Agilent Technologies) was used to monitor the MB concentration at the maximum absorbance wavelength of 665 nm and an Agilent Cary Eclipse Fluorescence Spectrophotometer was used to determine the concentration of hydroxyl radicals. The Total Organic Carbon (TOC) of the simulated synthetic wastewater was made using a TOC meter (Elementar Enviro, Germany). The degradation efficiency (η) was calculated by the change in concentration using Eq. (1):

$$\eta = \frac{C_0 - C_t}{C_0} \times 100 \tag{1}$$

where C_0 is the initial concentration (mg/L) and C_t is the concentration of MB (mg/L) at a given time t.

The specific energy consumption was evaluated using the electrical energy per unit order (EEO) concept. EEO is the electrical energy in kWh required to degrade a contaminant by one order of magnitude in a unit volume of wastewater [36]. EEO (in kWh/(m^3.order)) was calculated using Eq. (2):

$$EEO = \frac{U \times I \times t}{3600 \times V \times log_{10}\left(\frac{C_0}{C_t}\right)} \times 10^{-3} \tag{2}$$

where U is the cell voltage (V), I is the average current (A), t is the treatment time (s), and V is the volume of the treated wastewater (m^3), C_0 and C_t are the initial and final concentrations of methylene blue, respectively (mg/L).

All experimental measurements were performed in duplicate unless otherwise stated. Data are reported as mean values with the associated standard deviation (mean ± SD, n = 2), providing an indication of experimental variability and measurement reproducibility.

2.6 Analysis and identification of transformation products

The transformation products of methylene blue were analysed using an Agilent 1260 Infinity II HPLC system and an Agilent Ultivo triple quad mass spectrometer in ESI positive mode (LC-MS/MS). Nitrogen was used as sheath gas (11L/min, 250 ºC) and the fragmentor voltage was 135 V, which was optimised for methylene blue during the LC-MS/MS method development. The chromatographic separation was performed using a Phenomenex C18 column (100 mm×4.6 mm, 3 μm particle size), the mobile phase was 100 mM ammonium formate solution and acetonitrile in a ratio of 60:40, and the flow rate was 0.4 mL/min.

2.7 Degradation pathways

To investigate the electrochemical degradation pathways of MB, we performed LC-MS/MS analysis (Agilent 1260 Infinity II coupled with an Ultivo triple quadrupole mass spectrometer) alongside DFT calculations. LC-MS/MS was utilised to track the degradation products over time as the reaction progressed, while the DFT calculations identified potential reactive sites on the MB molecule where oxidants are likely to attack, based on Fukui functions. Fukui functions pinpoint the locations of reactive sites and, in their "condensed" form, offer a detailed description of chemical reactivity at the atomic level. The condensed Fukui functions, or Fukui indices, are defined by Equations (3-5).

$$f_i^- = q_i(N) - q_i(N-1) \tag{3}$$

$$f_i^+ = q_i(N+1) - q_i(N) \tag{4}$$

$$f_i^0 = \frac{1}{2}[f_i^- + f_i^+] \tag{5}$$

Where: f_i^- represents the Fukui index for electron removal from the molecule, also known as the Fukui index for electrophilic attack; f_i^+ is the Fukui index for electron addition to the molecule, also referred to as the Fukui index for nucleophilic attack; f_i^0 is the Fukui index for radical attack of the molecule; and q_i is the charge at atomic centre *i* for the molecule with *N* or *N*-1 or *N*+1 electrons. For a given type of reaction (i.e. electrophilic, nucleophilic, or radical), the atom with the highest Fukui index value is considered the most susceptible to attack. In this study, DFT calculations were performed using Gaussian 16W with Gaussian View 6.1 as the interface [37]. The molecular geometries were optimised using hybrid Density Functional Theory (DFT) with the B3LYP functional and the 6-31G basis set. Electron density and electron orbitals, such as HOMO and LUMO, were also obtained using Gaussian software. Active sites for radical attack were identified based on the Fukui indices f_i^0, calculated from Mulliken atomic charges derived from Gaussian analysis [38-40].

3 Results and discussion

3.1 X-ray diffraction analysis

Figure 2

The X-ray diffraction (XRD) patterns of the Ti, NiATOTi, and NiATOTiPt electrodes are shown in Fig. 2. According to Fig. 2(a) for Ti mesh, the most intense diffraction peaks centred at 40.11° belong to the standard Ti (101) planes and agree well with the standard Crystallography Open Database (COD) file (COD-9008517) of Ti. The other diffraction peaks are well matched with their corresponding standard Ti planes. This suggests that the Ti mesh has been properly annealed and has a pure Ti hexagonal structure. The presence of XRD peaks corresponding to Ni, Sb and SnO_2 in Fig. 2(b) for the NiATOTi electrode clearly reveal that Ti mesh was coated with Ni, Sb and SnO_2. The peaks related to Ni and Sb were low (Fig. 2(b)), possibly due to the strong signals from the SnO_2 since their diffraction angles are very close to those of SnO_2 [41]. The peaks observed at 35.07° and 45.61° correspond to the most intense peaks of Sb and Ni according to the standard COD file of Ni and Sb (Ni-1534892 & Sb-1539203), while the peak observed at 78.65° is related to both. The diffraction peaks centred at 38.38° and 40.16° belong to the standard Ti (002) and Ti (101) planes respectively. Here, only few peaks of Ti were obtained, which indicates that Ti is covered with the NiATO materials. The other peaks obtained are related to SnO_2 and are present in abundance. They are also well matched with the standard COD file of SnO_2 (COD-1000062). The XRD pattern of NiATOTiPt mesh (Fig. 2(c)) reveals the presence of the four elements Ti, Pt, Ni, Sb and SnO_2. The diffraction peaks centred at 39.38°, 45.98°, 80.74°, and 85.15° belong to the standard Pt (111), Pt (200), Pt (311) and Pt (222) planes respectively, indicating the presence of Pt [42-44]. Again, the peaks related to Ni (45.50°) and Sb (34.64°) were barely detected while the peaks for SnO_2 and Ti were present in abundance. In summary, the XRD pattern clearly demonstrates the respective phases of the electrodes. Ti and Sb have exhibited the hexagonal close-packed (hcp) structure, while Pt and Ni have demonstrated the face-centred cubic (fcc) structure, and SnO_2 has exhibited the tetragonal rutile structure.

3.2 SEM, Energy dispersive X-ray and Elemental mapping analysis

The SEM and EDS results of the pure Ti, NiATOTi, and NiATOTiPt electrodes are shown in Fig.3. Fig. 3(a-1) displayed the top view of the Ti mesh showing that the diameter of the mesh is approximately 123 μm with a clear rough surface [45]. Fig. 3(a-2) illustrates the surface of the NiATOTi electrode, demonstrating that the diameter of the mesh is approximately 127 μm. This evidence suggests that the NiATO solution coated the surface of the Ti mesh in a thickness of approximately 2 μm. Due to the coating of the NiATO solution on the surface of Ti mesh, the surface of NiATOTi electrode is coarse and rough [46]. Fig. 3(a-3) depicts the surface of the NiATOTiPt electrode showing that the diameter of the NiATOTiPt electrode is approximately 129 μm, which is greater than the diameter of the Ti mesh electrode and NiATOTi electrode. This observation strongly indicates the presence of a solution consisting of Pt and NiATO solution with a thickness of around 3 μm on the Ti mesh substrate in agreement with other studies [47].

According to Fig. 3(b-1), the EDS spectrum of the Ti mesh shows strong presence of Ti in the electrode which is corroborated by the elemental mapping of Ti mesh (Fig. 4(a)). The EDS spectrum of the NiATOTi electrode (Fig. 3(b-2)) and its elemental mapping (Fig. 4(b)) illustrate the presence of Ni, Sb, Sn on the surface of Ti mesh in NiATOTi electrode while these analyses revealed the presence of Pt in addition to the elements Ni, Sb, Sn on the surface of the NiATOTiPt electrode (Fig. 3(b-3) and Fig. 4(c)). These results of SEM, EDS and elemental mapping analyses confirm the presence of the expected elements of NiATO and Pt-NiATO on the surface of the titanium (Ti) mesh substrates and are in agreement with other studies [48, 49].

Figure 3

Figure 4

3.3 X-ray photoelectron spectroscopy (XPS)

Figure 5

The XPS analysis was performed to investigate the chemical and electronic structure, the oxidation state, and the surface chemical composition of the electrodes as well as the valence states of the different species. A wide scan XPS spectrum of Ti, NiATOTi and NiATOTiPt is shown in Fig. 5(a). The binding energies observed in the XPS spectrum were calibrated for specimen charging by referencing the C 1s to 284.8 eV [42, 50]. The photoelectron peaks of C, Pt, Ti, Ni, Sb, Sn and O were observed at their binding energies respectively. The XPS spectrum of carbon (C 1s) with four fitted peaks is shown in Fig. 5(b). It displayed two intense fitted peaks at 284.8 eV and 286.30 eV corresponding to C-C and C-OH bonds respectively. The first peak related to C-C due to the adventitious carbon and the second peak related to C-OH due to the hydroxyl bond [46]. The other small peaks at 287.80eV and 288.80 eV were attributed to carboxylate (O-C-O) and carbonyl (O-C=O) groups respectively [51, 52]. The percentages of these components in C 1s were confirmed to be 82.47 (C-C), 10.69 (C-OH), 2.22 (O-C-O) and 4.62% (O-C=O). The results in Fig. 5(c) demonstrates that the Ti 2p curves had a two-band structure. The presented Ti 2p spectra match well those of TiO_2 [53]. The spin-orbit splitting value for the Ti 2p is 5.7 eV in the oxide state. The main XPS peak of Ti centred at 458.81 eV corresponds to Ti $2p_{3/2}$, indicating the oxidised state of Ti and corresponds to Ti^{+2} state. The other peak observed at 464.51 eV reveals the presence of oxide component of Ti in the form of Ti $2p_{1/2}$ and belongs to Ti^{+2} state [46, 54]. Generally, the Full Width at Half Maximum (FWHM) for the component of an element is the same, but for Ti 2p it is not because the Ti $2p_{1/2}$ component is much broader than the Ti $2p_{3/2}$ component. The percentage components of Ti $2p_{3/2}$ and Ti $2p_{1/2}$ are 65.23 and 29.10% respectively, which is close to a ratio of

2:1. A very small peak at 454.33 eV is associated with the pure Ti $2p_{3/2}$ metal [55, 56]. For the Ti metal, the spin-orbit splitting value is 6.1 eV, so the other component of the Ti metal is obtained at 460.33 eV, which is the Ti $2p_{1/2}$ metal [56]. The percentages of the metal components of Ti $2p_{3/2}$ and Ti $2p_{1/2}$ are 3.76 and 1.89% respectively, which is again in the ratio of 2:1.

Looking at the wide scan XPS spectrum of NiATOTi electrode in Fig. 5(a), the peaks related to C 1s, O 1s, Sb 3d, Ti 2p, Ni 2p, and Sn 3d are observed. The most intense peaks are correlated to C, Ti, O, and Sn. The XPS spectra of Ni, Sb and Sn are shown in Fig. 5(d), (e) and (f) respectively. The amount of $NiCl_2$ and $SbCl_3$ was quite low compared to $SnCl_4$ used for the synthesis of the NiATO solution. Therefore, it was very difficult to detect Ni and Sb in the XPS spectrum compared to Sn [57]. The fitted XPS spectrum of O 1s and Sb 3d is presented in Fig. 5(e). It is well known that XPS spectrum of Sb $3d_{5/2}$ can not be used to detect the oxidation state of Sb, because the Sb $3d_{5/2}$ peak overlaps almost perfectly with the O 1s peak. Thus, generally Sb $3d_{3/2}$ peak is used for the determination of the valence of Sb. The spin-orbit splitting for the oxide component of Sb 3d is ~ 9.4 eV, the peak obtained at 530.98 eV can be designated as Sb $3d_{5/2}$ while a tiny peak obtained at 541.03 eV strongly reveals the presence of Sb $3d_{3/2}$ [48]. The other fitted peak at 530.62 eV corresponds to the metal oxide of O 1s and the fitted peak centred at 532.52 eV corresponds to the hydroxide of O 1s [50]. The XPS spectra of Ni and Sb of NiATOTi electrode support the result obtained from XRD, EDS and elemental mapping. The fitted XPS spectrum of Sn 3d is demonstrated in Fig. 5(f). It distinctly reveals a two-band structure in the XPS spectrum of Sn 3d. The spin-orbit splitting value for the Sn 3d is 8.4 eV. The peaks of Sn 3d are symmetrical and located at 486.60 and 495.0 eV, corresponding to the oxides of Sn $3d_{5/2}$ and Sn $3d_{3/2}$, respectively [48, 56]. The percentages of Sn 3d components are 60.31 (Sn $3d_{5/2}$) and 39.69 % (Sn $3d_{3/2}$), respectively.

The wide-scan XPS spectrum of NiATOTiPt illustrated in Fig. 5(a) reveals the presence of peaks corresponding to C 1s, O 1s, Sb 3d, Ti 2p, Pt 4f, Ni 2p, and Sn 3d. The fitted XPS spectrum of Pt 4f consists of three peaks and is presented in Fig. 5(g). The peak at 71.0 eV indicates the presence of metallic Pt 4f and corresponds to Pt $4f_{7/2}$. The spin-orbit splitting value is 3.35 eV for Pt 4f, whereas the other peak at 74.35 eV represents the presence of metallic Pt $4f_{5/2}$. The broad peak obtained at 76.2 eV corresponds to $Pt(OH)_2$ or PtO_2, possibly due to the adsorption of contaminants that react with Pt to form these species [57]. We again observed that the XPS spectra of Ni were absent. The fitted XPS spectrum of Sb 3d is displayed in Fig. 5(h). The peak located at 532.4 eV corresponds to Sb $3d_{5/2}$. The spin-orbit splitting value for the Sb 3d is 9.4 eV and the other peak, obtained at 541.02 eV, clearly depicts the presence of Sb $3d_{3/2}$. The peak obtained at 537.83 eV between the two peaks of Sb 3d seems to be due to the satellite function of Sb and is defined as Sb $3d_{5/2}$ satellite [50, 58]. The other peaks centred at 532.8 eV and 534.8 eV belong to O1s, representing the lattice oxide and organic C=O bonds of O1s respectively. Fig. 5(i) shows the fitted XPS spectrum of Sn 3d. It again demonstrates the two band structure due to the spin-orbit splitting of Sn 3d that were discussed for the NiATOTi electrode. Both peaks are symmetrical and correspond to Sn $3d_{5/2}$ and Sn $3d_{3/2}$ respectively. Overall, the XPS analysis of all electrodes showed a good correlation with the results of XRD, EDS and elemental mapping.

3.4 FTIR Analysis

Figure 6

Following confirmation of catalyst formation on the Ti mesh as demonstrated in the previous sections, Fourier Transform Infrared (FT-IR) spectroscopy was conducted to identify the surface functional groups present on all electrodes after the degradation of the MB solution. The FTIR spectrum of the Ti mesh shows that only a few peaks are observed (Fig. 6). The characteristic peak of metal-oxygen stretching appeared at 577 cm^{-1}, which is obtained in all FTIR spectra of the electrodes [59]. The peak appeared at 773 cm^{-1} corresponds to C-H bending. The peak observed at 1047 cm^{-1} is related to the stretching of the C-OH group while the peaks at 2125 cm^{-1} correspond to the C=O anhydride [59].

The peaks in the FTIR spectra of NiATOTi and NiATOTiPt are observed at almost the same positions. The C-OH stretching is responsible for the peak centred at 1047 cm^{-1} [54] and the peaks at 1396 cm^{-1} belong to the $-CH_3$ bending, respectively [54] . The peak obtained at 2125 cm^{-1} belong to the C=O aldehyde [60, 61]. The symmetric and asymmetric stretching vibrations of the -C-H and =C-H groups were identified at 2895 and 2981 cm^{-1}, respectively [62, 63]. Two other sharp peaks appeared at 3670 cm^{-1} and 3741 cm^{-1} correspond to -OH stretching [1, 59, 60]. In general, the FTIR spectrum of all electrodes reveal the presence of functional groups on the surface of the electrodes formed during the degradation of MB.

3.5 Reactive species generation

Amongst the various reactive species generated in electrochemical systems, $^{\bullet}$OH radicals and ozone are the most important oxidative species responsible for the degradation of organics [64, 65]. Therefore, the efficiency of the electrodes to generate these two important oxidants in water was evaluated. The reactor was run in a closed-loop circulating mode, the applied voltage was 5 V, and the circulation flow rate was 88.5 mL/min.

3.5.1. Hydroxyl radicals

The three electrodes were evaluated for $^{\bullet}$OH generation using disodium-terephthalic acid (Na$_2$TPA) as a probe molecule for the measurement of $^{\bullet}$OH [64, 65]. Na$_2$TPA reacts with $^{\bullet}$OH to produce a highly fluorescent product, 2-hydroxy-terephthalate (OHTPA), which was measured by the Fluorescence Spectrophotometer using a preliminary determined calibration curve. The optimised excitation and emission wavelengths for OHTPA were found equal to 312 and 426 nm, respectively (Fig. 7(a)). Assuming a 35% yield of the reaction of Na$_2$TPA with hydroxyl radicals [64, 66], the concentration of $^{\bullet}$OH ([$^{\bullet}$OH]) was estimated as $[^{\bullet}\text{OH}] = [\text{OHTPA}]_{\text{meas}}/\text{yield}$; where $[\text{OHTPA}]_{\text{meas}}$ is the measured concentration of OHTPA and yield is the yield of the reaction (i.e. 35%).

Figure 7

Fig. 7(b) shows that for all three electrodes, $^{\bullet}$OH concentration increased linearly initially before it plateaued for the Ti and NiATOTi electrodes. The NiATOTiPt clearly shows a higher production of $^{\bullet}$OH in comparison to the other two electrodes and did not exhibit significant slowing of the $^{\bullet}$OH production within the time of 120 minutes. Running the experiments for longer times showed that, for all three electrodes, $^{\bullet}$OH concentrations reached maxima before declining as time increased (data not shown). The $^{\bullet}$OH production rates of the initial part of the curves for each electrode, determined from the slope of the tangent lines displayed in Fig. 7(b), are shown in Fig. 7(c). The $^{\bullet}$OH production rate is minimum for the Ti mesh (0.8902 nmol/(L.min)) but was maximum for the NiATOTiPt electrode (1.9746 nmol/(L.min)). This clearly shows that the most efficient electrode for the production of hydroxyl radical is NiATOTiPt. As observed in Fig. 3, the introduction of Pt to the composition of the electrode produced a homogeneous surface without cracks, improving the grain sizes and crystallinity of the catalyst, which lowers the charge transfer resistance [16]. In electrochemical oxidation, lowering the resistance to charge transfer facilitates faster electron transfer, leading to an increase in the production of hydroxyl radicals [67, 68], which explains the higher $^{\bullet}OH$ production rate observed for NiATOTiPt.

3.5.2. Ozone Analysis

The formation of ozone in the electrochemical cell was evaluated in neutral media using pure Milli-Q water and different conductivities of 0.25, 1.5, and 9.82 µs/cm set by addition of $NaNO_3$ solution. Ozone concentration was measured using the gravimetric indigo method [69, 70]. The results showed that no ozone was detected. The production of ozone via electrochemical means using the NIATO-based electrodes is possible but it requires the use of corrosive acidic H_2SO_4 electrolytes [71]. Rapid deactivation of the electrodes has also been reported and is considered one of the barriers for the commercialisation of these electrodes for electrochemical ozone production [71].

3.6 Electrochemical degradation of methylene blue

3.6.1 Efficiency of the three electrodes for MB degradation

Figure 8

The degradation of MB was compared across the three electrodes (Ti, NiATOTi, and NiATOTiPt) under identical operating conditions (voltage of 5 V, and a circulation flow rate of 88.5 mL/min). Fig. 8 (a-c) illustartes the changes of the UV/Vis spectra as function of time using the three electrodes. According to this figure, all three anodes degraded MB, though at different efficiencies and rates. The time required for a degradation percentage of 95% (t_{95}) was 130 min for the Ti electrode while NiATOTi and NiATOTiPt electrodes required 70 and 50 minutes, respectively. To further illustrate the efficiency of the electrodes and compare their performances, the values of the pseudo-first-order reaction rate constant, *k*, were determined by fitting the experimental results to a first-order model (i.e. C/C_0 =exp(-kt)). The model fitting results shown by continuous lines in Fig. 8(d) indicate excellent agreement between the experimental and model results. Fig. 8(e) shows that at the used voltage of 5 V, the rate constants varied between 0.0229 min^{-1} to 0.0616 min^{-1} for the three electrodes. At this voltage, the rate constant, *k*, of NiATOTi electrode was twice that of the Ti electrode while NiATOTiPt displayed a rate constant of 2.6 times higher than the Ti electrode (or 1.3 times higher than NiATOTi). These results suggest that the NiATOTiPt electrode is the most efficient out of the three electrodes, which agrees well with our previous findings that showed NiATOTiPt electrode exhibited the highest $^\bullet$OH production rate due to its improved grain size and crystallinity as a result of the introduction of Pt. To further support this finding, we plotted the change of the degradation rate constant, *k*, as function of the production rate of $^\bullet$OH, R_{OH}, of each electrode. As shown in Fig. 8(f), an excellent linear relationship between *k* and R_{OH} was found. It can thus be concluded that $^\bullet$OH plays a key role in the degradation of MB by EAOP.

To evaluate performance, we compared the pseudo-first-order rate constants (*k*) obtained in this study with those reported in the literature for Ti/Sb-SnO_2-based and modified electrodes used in the degradation of dyes and other organic pollutants. A summary of these literature values is provided in Table S2 and Fig. S1 (Supplementary Information). As shown in Fig. S1, 59% of the k-values reported in the literature fall within the range of 0.03-0.06 min^{-1}, which is consistent with the values obtained in our study. The observed outliers below and above this range are likely due to variations in electrode composition, fabrication methods, or operating conditions. For example, Zhang, et al. [30] reported pseudo-first-order rate constants for MB degradation using Sb-SnO_2-based electrodes ranging from 0.003 to 0.028 min^{-1}. Their most effective electrode, TiO_2-NiO@Sb-SnO_2, achieved its highest efficiency primarily due to the incorporation of NiO, which enhanced the fraction of adsorbed hydroxyl oxygen species, improved charge transfer between the electrolyte and electrode, and increased both the oxygen evolution potential (OEP) and the electrode's surface area [30]. Ce-doped Ti/SnO_2-Sb electrodes prepared by electrodeposition with glucose in the plating solution achieved higher methylene blue degradation rates than those prepared without glucose, with rate constants ranging from 0.079 to 0.147 min^{-1} [5]. The enhanced efficiency was attributed to the addition of glucose at the fabrication stage of the electrode, which increased the oxygen evolution overpotential and generated a highly porous structure, thereby providing more active catalytic sites. The studies further demonstrate that the addition of NaCl as an electrolyte enhances the degradation rate constants through the generation of active chlorine species [72, 73], while increasing the current density or the applied potentiostatic voltage also leads to higher degradation rate constants (this study and [5]). The addition of other metals to the composition of the electrode such as Gd, Ru, or La also enhances the rate constant [74, 75]. The effect of the operating conditions on the efficiency of our electrodes evaluated in this study is discussed next.

3.6.2 Effect of Voltage

Figure 9

The impact of voltage on methylene blue (MB) degradation using Ti, NiATOTi, and NiATOTiPt electrodes was analysed by varying the voltage from 1.2 V to 10 V, while maintaining a constant circulation flow rate of 88.5 mL/min in both electrode compartments. The results are presented in Fig. 9. For clarity of the figure, the time axis in Fig. 9 extends to 90 minutes only, though in some cases, the experimental duration was longer to ensure that at least 95% of the dye was degraded. For the Ti electrode, the required time to achieve 95% degradation (t_{95}) (i.e. $C/C_0 = 0.05$) was 240 minutes at 1.2 V but as the voltage increased to 10 V, t_{95} fell to 90 minutes. A similar trend was also observed for the NiATOTi and the NiATOTiPt electrodes where t_{95} was reduced from 180 min and 140 min at 1.2 V to only 50 min and 20 min at 10 V, respectively. Thus, the higher the applied cell voltage, the faster the degradation of MB, which is clealry shown by an upward correlation between the increased voltage and the rate constants of MB degradation, *k*, for all electrodes (Fig. 9(d)). As shown in Fig. 9(d), the NiATOTiPt electrode exhibited the fastest degradation rates compared to the NiATOTi and Ti electrodes at the tested voltages. For instance, at a voltage of 10 V, the rate constant of NiATOTiPt is 7.5 and 3.3 times higher than that of Ti and NiATOTi, respectively. The results indicate that higher voltages enhance the electrochemical reactions at the anode by increasing the generation of reactive species (i.e. hydroxyl radicals). As the voltage rises, the electrical energy driving the oxidation process strengthens, potentially leading to the production of additional oxidising agents such as ozone and hydrogen peroxide, which react to further generate hydroxyl radicals via the peroxone reaction:

$$H_2O_2 + 2\,O_3 \rightarrow 2\ {}^{\bullet}OH + 3O_2 \tag{6}$$

Higher voltage also improves the rate of electron transfer at the electrode surface and raises the current density, accelerating the oxidation process by increasing the number of active sites available for the oxidation reactions [23].

In Fig. 9(d), the effect of voltage was most pronounced with the NiATOTiPt electrode. As the voltage increased from 1.2 V to 10 V, the rate constant increased by 11 times for NiATOTiPt, while it increased by 4 and 2 times for the NiATOTi and Ti electrodes, respectively. Thus, the incorporation of Pt into the electrode composition significantly enhanced the electrochemical oxidation process for MB degradation at high voltages, possibly due to its high catalytic properties and stability [76, 77]. These results demonstrate the superior performance of the Pt-containing electrode. Although platinum addition is expected to increase electrode material costs, it was used here at very low loading and delivered a high improvement in degradation kinetics and energy efficiency, as demonstrated by the EEO analysis in the next paragraph. Beyond its catalytic activity, Pt is biocompatible and chemically stable, with strong resistance to oxidation and long-term degradation. Such performance gains may justify the use of Pt-modified electrodes in targeted applications where treatment efficiency is required, including (i) polishing steps for textile or specialty chemical effluents to meet stringent discharge limits, (ii) on-site or decentralised treatment systems where reduced reactor footprint and shorter treatment times are required, (iii) treatment of low-volume wastewaters containing recalcitrant organic pollutants, and (iv) water reuse schemes where enhanced oxidation performance is needed to ensure consistent contaminant removal.

The electric energy per order (EEO) was calculated for both the NiATOTi and NiATOTiPt electrodes, with the results shown in Fig. 9(e). The data reveals that, for voltages below 8V, EEO increased almost linearly with voltage up to 0.74 and 0.48 kWh/(m^3.order) for NiATOTi and NiATOTiPt, respectively. Furthermore, at every voltage level, NiATOTi exhibited higher EEO compared to NiATOTiPt, suggesting that NiATOTiPt is a more energy-efficient electrode. For instance, at 8V, NiATOTiPt required 35% less energy than NiATOTi. In all cases, both electrodes in this study demonstrated EEO values of less than 1 kWh/(m^3.order), highlighting their potential for advanced water treatment applications [78]. Based on data related to the electrochemical oxidation of MB by electrodes made of TiO_2-NiO@Sb-SnO_2 and TiO_2@Sb-SnO_2, reported by Zhang, et al. [30], EEO values of 1.37 and 2.58 kWh/(m^3.order), which are closer to our results, were calculated. The incorporation of co-dopant NiO into the electrode structure has also significantly enhanced energy efficiency [30], consistent with our findings that introducing Pt into the electrode composition likewise improved the energy efficiency of the electrochemical process. In contrast, other research studies have reported significantly higher EEO values for their electrochemical processes using mixed-metal oxide electrodes. For example, Xu, et al. [79] have reported an EEO value of 6.55 kWh/(m^3.order) for the synchronous degradation of three non-steroidal anti-inflammatory drugs, while Zhang, et al. [80] reported EEO values of 29.5 kWh/(m^3.order) for the electrochemical treatment of a textile wastewater. In their study on EEO for the boron-doped diamond (BDD) electrode, Lanzarini-Lopes, et al. [81] reported EEO values for the degradation of *p*-chlorobenzoic acid ranging from 39.3 to 331.8 kWh/(m^3.order). Yang, et al. [82] reported an EEO of 10.22 kWh/(m^3.order) for the elimination of Orange G dye using a conventional BDD electrode. By developing a porous BDD electrode, they were able to significantly reduce the EEO of the dye degradation to 2.59 kWh/(m^3.order) [82]. Electrochemical oxidation of C.I. Acid Blue 92 using a BDD anode under recirculation flow mode, comparable to the flow mode of our setup, required an EEO of 55.95 kWh/(m^3.order) [83], significantly higher than the EEO in our study. Although BDD is widely regarded as the benchmark electrode for electrochemical oxidation because of its exceptional stability, excellent electrical conductivity, and wide potential window, its practical application is limited by the high fabrication cost and energy demand [82]. The energy consumption typically reported for BDD is higher than the values obtained in this study, highlighting the advantage of our system in terms of energy efficiency while maintaining effective degradation performance. Nevertheless, considering various types of electrodes, a wide variability over three orders of magnitude in EEO has been reported for textile dyes, with values ranging from below 1 to >1000 kWh/(m^3.order), this study and [80, 82, 83]. This variability can be explained by variability in the generation of electrochemical oxidants, electrode materials, reactor configuration, or the composition of the water matrix used [66, 77, 84, 85].

The production of reactive species such as hydroxyl radicals or active chlorine directly affects degradation kinetics [86], thereby reducing EEO by accelerating pollutant removal. Electrode materials are crucially important, as their catalytic activity, stability, and oxygen evolution overpotential determine current efficiency and thus energy demand. As demonstrated so far, BDD electrodes usually achieve faster degradation but at higher energy costs compared to mixed-metal oxides or doped composites. Water composition, particularly ionic strength, pH, and the presence of natural organic matter or inorganic scavengers, can either promote oxidant formation (e.g., via chloride or sulphate activation) or consume reactive species, thereby influencing degradation efficiency and the corresponding EEO values [86-88]. In addition, reactor configuration strongly influences the energy consumption of electrochemical degradation of pollutants. Flow-through and continuous-flow reactors generally achieve lower energy per order (EEO) than batch systems due to enhanced mass transport and improved pollutant-electrode contact. Optimised cell design, such as reduced inter-electrode distance and improved hydrodynamics, further minimises energy consumption by lowering ohmic losses, enhancing current efficiency, and reducing mass transfer limitations of the contaminants toward the electrode surface [11, 88]. While our electrode and reactor configuration (i.e. flow through mode) demonstrate considerable energy savings, further testing with more complex, real-world wastewaters is necessary to fully evaluate the efficiency of the system. Nevertheless, the results of this study are promising, suggesting that NiATOTiPt electrode has great potential for textile dye degradation applications.

3.6.3 Effect of pH

pH plays an important role in the electrochemical degradation of contaminants because it influences, at a minimum, contaminant speciation and the availability of reactive oxidants such as $^\bullet$OH, HOCl, and OCl$^-$ [85]. Thus, the effect of pH on the performance of NiATOTiPt was evaluated. The pH-dependent experiments in Fig. 10 show that NiATOTiPt electrode was active across the pH range investigated (pH 5 to 9.5), but the degradation rate of MB slightly varied as the pH was changed. In all cases, C/C_0 decreased monotonically with time and fell to ~0.1 after 60 min, indicating significant decolourisation under mildly acidic, neutral and alkaline conditions. The curve at pH 5 consistently lied below the others, demonstrating that slightly acidic conditions lead to faster MB removal. This trend is further supported by the variation in the pseudo-first-order rate constant, expressed as k/k_{pH5}, shown in the inset of Fig. 10. The change of C/C_0 versus time at pH 7 is only marginally slower and almost overlaps that at pH 8.5, suggesting that near-neutral to mildly alkaline conditions do not strongly reduce performance. In contrast, at pH 9.5, C/C_0-values are slightly higher at 30 to 60 min, with noticeably reduced rate constant (inset of Fig. 10), showing that strongly alkaline solutions reduce the degradation rate. A similar behaviour was reported for an electro oxidation system using particle electrodes, where MB removal was significantly reduced at pH 11[1]. Alaoui, et al. [89] also reported that MB degradation by Pt/MnO_2 electrode decreased as the pH was increased to 10. At higher pH, the onset potential for oxygen evolution shifts to lower values, promoting oxygen evolution at the anode surface and consequently hindering the diffusion of organic species toward the electrode [89], reducing contaminant degradation. In our study, the pseudo-first-order rate constants quantify this trend, as k/k_{pH5} increases from 0.75 at pH 9.5 to ~0.90 at pH 7-8.5 and reaches a maximum of 1 at pH 5, i.e. the process at pH 5 is ~25 % faster than at pH 9.5. Hassan and Jamal [90] reported that, in chloride media, the indirect oxidation of MB on Pt exhibits a rate constant that increases linearly as pH decreases below 7. Likewise, Vahid and Khataee [83] observed slower degradation of acid blue 92 under alkaline conditions, with the rate constant at pH 8.5 reduced by approximately 15% compared with that at pH 6.

The effect of pH on the EEO was also examined in our study. At pH 7, the EEO decreased by approximately 30% relative to pH 5, yet remained about 20% higher at pH 9.5 than the value at pH 5. This behaviour aligns with the findings of Vahid and Khataee [83], who reported that EEO values (normalised to that at pH 6) increased by about 80% at pH 3.5 and by 15% and 20% at pH 8.5 and 11, respectively. These results clearly demonstrate that pH has a major impact not only on reaction kinetics but also on the overall energy demand of the process. Importantly, higher reaction rate constants do not necessarily translate into lower energy consumption, as pH can intensify competing side reactions such as oxygen evolution, or impact contaminant-electrode interactions and mass transfer [91]. Therefore, when energy performance is critical, careful optimisation of pH is essential.

Figure 10

3.6.4 Effect of circulation flow rate

Figure 11

The impact of circulation flow rate on the degradation efficiency of methylene blue was assessed at a constant voltage of 5 V in a closed-loop mode for all electrodes. As shown in Fig. 11(a), the pseudo-first-order rate constant initially increased with the flow rate, peaking at approximately 123 mL/min for Ti and NiATOTiPt, and at 148 mL/min for NiATOTi before decreasing as the flow rate further increased. Although charge transfer is typically the rate-limiting step in electrochemical processes, mass transfer is likely to dominate the reaction rates under the relatively high voltages used in the electrochemical cell of our study [92]. As the flow rate increased from 44 mL/min to 123 mL/min, the Reynolds number (Re) also rose from about 150 to 450, indicating enhanced mass transfer [93]. This increase in Re likely contributed to the observed rise in the rate constant, as mass transfer governs the supply of reactants and the removal of products at the active sites, thus directly influencing catalytic performance [94]. Consistent with this, Wang, et al. [95] demonstrated that increasing flow rates improved mass transfer and, in turn, the performance of a desalination electrochemical flow battery. However, as Fig. 11(a) illustrates, further increasing the flow rate beyond about 123 mL/min for Ti and NiATOTiPt and 148 mL/min for NiATOTi led to a decrease in the degradation rate constant. At high flow rates, flow channelling was observed to become significant, leading to dead zones and incomplete contact between the electrode and the liquid. This resulted in a reduced effective surface area of the electrode and, consequently, a decline in the observed rate constant. Excluding the flow rates that caused channelling, power was measured, and the EEO values as a function of flow rate for both the NiATOTi and NiATOTiPt electrodes are presented in Fig. 11(b). The figure demonstrates that as the flow rate increased, which enhances mass transfer, the EEO values decreased, indicating that the energy demand of the electrochemical process was reduced. This finding aligns with results from other studies [94, 95] and further reinforces our conclusion that mass transfer influences the electrochemical process.

3.6.5 Electrode reusability

Electrode stability is a significant factor in electrochemical systems, as it determines the durability and reusability of the catalytic surface. Reductions in catalytic performance after multiple uses of electrodes have been widely reported and are often linked to mechanical damage, crack formation during repeated use, passivation of the metal substrate, coating detachment, or gradual depletion of the active layer [5, 77]. Highly oxidising radical species may also induce partial oxidation of transition-metal nanoparticles [96] and the accumulation of degradation by-products on the nanostructured surface can progressively hinder the mass transfer of contaminants and reactive oxidants, contributing to the loss of activity [97]. To mitigate electrode deactivation, several strategies have been proposed, including TiN doping, glucose addition, and the fabrication of denser surface architectures, which collectively strengthen the coating, suppress crack development, slow catalytic layer dissolution, and delay substrate passivation, thereby enhancing electrode stability [5, 67, 98, 99]. In our study, stability was assessed by repeatedly reusing the NiATOTiPt electrode for the degradation of fresh MB solutions over multiple operational cycles. The study demonstrated a slight decline in catalytic activity across four consecutive cycles as shown in Fig. S2 (Supplementary Information). The concentration profiles show that MB degradation efficiency declines slightly with each successive cycle. In the first run, the electrode reduces MB from about 9.8 mg/L to 0.75 mg/L within 60 minutes. By the fourth run, however, the final concentration after 60 minutes was closer to 1.5 mg/L, indicating a modest loss in catalytic activity. Notably, after completing these four cycles and storing the electrode in DI water, a second set of four-cycle tests was performed again. Surprisingly, the electrode achieved degradation rates nearly identical to those observed in the initial set of cycling tests, indicating that its catalytic efficiency was effectively restored and that the slight performance loss observed in the first cycling test was not permanent. The average pseudo-first-order rate constant from the first set of cycling tests was only about 8% higher than the average pseudo-first-order rate constant obtained in the second set of cycling tests. The restoration of catalytic efficiency is likely due to the removal of surface-adsorbed intermediates or reaction byproducts during storage in DI water. During repeated degradation cycles, organic residues or oxidised species can accumulate on the electrode surface, partially blocking active sites and slowing electron-transfer processes. Immersion in DI water facilitates desorption or dissolution of these species, effectively regenerating the active surface of the NiATOTiPt electrode. As a result, the electrode regains its original reactivity, leading to the recovery of degradation rates comparable to those observed in the initial cycles. Potential loss of catalytic metals was assessed by analysing the treated solutions for dissolved metal species using an Agilent MP-AES following the electrochemical stability experiments. No electrode-derived metals were detected within the analytical detection limit (~0.5 μg/L), indicating negligible leaching. This result suggests good coating adhesion under the applied operating conditions, supporting the conclusion that no significant material loss or coating detachment occurred during the cycling tests. Nevertheless, it should be noted that over extended operational periods, there remains the potential for antimony and platinum leaching. In particular, antimony release is of concern due to its associated toxicity and the relatively low drinking water guideline value of 5 μg Sb/L [100], highlighting the importance of long-term stability assessments for practical applications, especially when treated water is intended for potable use or discharge into sensitive environmental receptors. Thus, it can be inferred that NiATOTiPt did not experience mechanical degradation or passivation during repeated use, and that a simple cleaning step between cycles is sufficient to restore the electrode to its original efficiency.

3.6.6 Treatment of simulated methylene blue synthetic textile wastewater

The electrochemical cell was evaluated for the treatment of a simulated methylene blue synthetic textile wastewater (MB_STWW), with the composition detailed in Table S1. This matrix was designed to reflect the practical relevance of anodic oxidation under realistic conditions, incorporating a complex, salt-rich, and organic-loaded environment typical of textile effluents. For comparison, a methylene blue solution prepared in deionized water (MB_DI) was also tested as a control to benchmark system performance against that obtained with MB_STWW. This comparison was particularly important given that the electrode had been extensively used prior to these experiments, allowing potential matrix effects to be distinguished from electrode aging effects. According to Fig. 12, both matrices (MB_STWW and MB_DI) followed pseudo-first-order kinetics for MB degradation, consistent with the previous results and common observations in oxidative degradation processes in which the oxidant concentration is effectively constant or proportional to the applied current [11]. The pseudo-first-order rate constant obtained for MB_STWW was 64% higher than that for MB_DI. Over a 60-minute treatment period, the concentration ratio C_t/C_0 decreased from 1.0 to approximately 0.01 for MB_STWW, compared to about 0.1 for the MB_DI solution (Fig. 12). The apparent faster decay in the simulated textile matrix is attributed to the higher ionic strength from the supporting electrolytes that promote higher cell currents and corresponding higher electrogenerated hydroxyl radicals or mediated oxidant flux at the anode surface [101]. Additionally, the presence of chloride and other anions under anodic conditions is associated with the production of active chlorine species that accelerate colour removal [72]. The accompanying effect is a higher pseudo-first-order rate constant for the dye disappearance.

Notwithstanding the faster dye degradation kinetics in the MB_STWW matrix, the energetic requirements of treatment, as estimated by the EEO of MB degradation was few orders of magnitude higher for MB_STWW than for MB_DI control. For MB_STWW, the average EEO was about 8.4 kWh/(m^3.order), whereas for MB_DI, the average EEO was 0.17 kWh/(m^3.order). Although the EEO for MB_STWW is substantially higher than that obtained for MB_DI, the absolute value remains within a practically acceptable range for advanced oxidation processes. Reported benchmarks indicate that EEO values below 10 kWh/(m^3.order) are generally considered energetically feasible for water and wastewater treatment applications, particularly for complex matrices containing salts and organic matter [78]. This increase in energy demand for MB_STWW can be attributed to the higher ionic strength and organic load of the simulated textile wastewater, which promote the formation of secondary oxidants and competitive reactions with species such as humic acid and polyvinyl alcohol that reduce the fraction of applied current available for direct dye oxidation. Overall, the EEO value achieved by the NiATOTiPt electrode for the treatment of the MB synthetic wastewater (8.4 kWh/(m^3.order)) remains lower than many values reported for boron-doped diamond (BDD) electrodes, which are often regarded as the benchmark for electrochemical oxidation. For example, EEO values of 10.22 kWh/(m^3.order) for Orange G dye [82], 55.95 kWh/(m^3.order) for C.I. Acid Blue 92 [83], and 39.3-331.8 kWh/(m^3.order) for *p*-chlorobenzoic acid [81] have been reported using BDD anodes.

Total organic carbon (TOC) measurements indicated limited mineralisation in both water matrices, with approximately 8% removal achieved. In the MB_STWW system, TOC decreased from 272.7 mg/L to 251.4 mg/L after 60 minutes of treatment, while in the MB_DI solution, TOC was reduced from 30.1 mg/L to 27.9 mg/L over the same reaction period. The extent of TOC removal, despite a near-complete MB decolouration, indicates that the electro-oxidation predominantly affected chromophore destruction and fragmentation rather than complete mineralisation to carbon dioxide and water. This pattern is common in electrochemical AOPs treating complex aqueous matrices; colour and parent compound disappearance can be fast, while complete mineralisation is substantially slower because of low molecular weight intermediates and other fractions [102, 103].

Figure 12

3.7 Pathways of MB degradation by NiATOTiPt electrode

The degradation of methylene blue (MB) was conducted with an initial concentration of 100 µg/L, while maintaining the following conditions: a voltage of 10V, a circulation flow rate of 88.5 mL/min, and a solution volume of 125 mL in a closed-loop system. Fig. 13(a) depicts the molecular structure of MB, excluding its chloride ion, which is solvated by water once the dye is dissolved in solution. This structure was optimised using DFT analysis in Gaussian. The mass-to-charge ratio (*m/z*) of MB excluding Cl is 284, corresponding to the molecular ion [M^+], as observed in our study and corroborated by previous research [104, 105]. Fig. 13(g) (MB, *m*/*z* 284) illustrates the progression of the electrochemical degradation of MB over time, showing a consistent decrease in MB concentration. However, after approximately 15 minutes, the concentration plateaued at around 20 µg/L, representing an 80% removal (Fig. 13(g) (MB, *m*/*z* 284)). This suggests that the electrochemical degradation of MB did not proceed beyond this point. While the initial decline in concentration before the plateau aligns with trends observed for higher initial MB concentrations, the plateau was not detected using the UV/vis spectrophotometer. This discrepancy is likely due to the higher limit of detection (LOD) of the UV/vis spectrophotometer (approximately 100 µg/L) compared to the mass spectrometer, which has a lower LOD of about 30 ng/L. The observed plateau in Fig. 13(g) (MB, *m*/*z* 284) may be attributed to competition reactions involving by-products formed during MB oxidation, or it could indicate inhibition of the electrochemical process at low MB concentrations.

To elucidate the electrochemical degradation pathway of methylene blue (MB) using the NiATOTiPt electrode, LC-MS/MS analysis (Agilent 1260 Infinity II with Ultivo triple quadrupole) and DFT calculations were performed. The degradation of the MB molecule by the NiATOTiPt electrode is primarily attributed to hydroxyl radical attack, as previously demonstrated in this study. To identify the most reactive sites for radical attack on the MB molecule, Fukui functions (f^0) were employed. Fig. 13(f) illustrates a plausible mechanism for the electrochemical degradation of MB by the NiATOTiPt electrode suggested according to the following discussion while Fig. 13(g) illustrates the changes in normalised peak area of each by-product, represented by its *m*/*z* value. In Fig. 13(g), the normalised peak area is defined as the ratio of the peak area of a given *m*/*z* to the peak area of MB (*m*/*z* 284) at time t = 0, multiplied by 100. Fig. 13(a-e) presents the molecular structure of MB along with its HOMO and LUMO orbitals, as well as the f^0 function map and indices. The HOMO and LUMO orbitals indicate the regions where a molecule is most likely to lose or gain electrons, respectively. The HOMO map of MB (Fig. 13(c)) highlights regions of high electron density, where the likelihood of electron participation in the oxidation reaction is greatest. In oxidation reactions, electron transfer typically occurs from the HOMO of the organic molecule to the LUMO of the oxidant [106, 107]. The f^0 function map identifies the sites most likely to undergo radical attack. Fig. 13(e) presents a descending order of the f^0 indices, suggesting that C16, C19, C20, and C17 in the MB molecule are the most susceptible to hydroxyl radical reactions, followed by C1, C13, C3, and C11.

Figure 13

The attack of hydroxyl radicals ($^\bullet$OH) on C16 (or C19, C20, and C17) leads to N-demethylation of the -CH_3 group attached to the nitrogen atom in the methylene blue (MB) molecule. The N-demethylation pathway at C16 is shown in Scheme 1 of Fig. 13(f), resulting in the formation of product **P1** (*m/z* 270). Further demethylation produces products **P2** & **P2'** (*m/z* 256), **P3** (*m/z* 242), and **P4** (*m/z* 228). The cleavage of a methyl group substituent from amine groups via radical oxidation has also been observed in other studies [108-110]. Demethylation of **P1** occurs at N15 and/or N18, resulting in two isomers, **P2** and **P2'**. To determine which isomer predominates, we calculated the Fukui function f^0 for **P1**. The results show that the Fukui indices for C16 (0.0166), C17 (0.0164), and C19 (0.0162) are comparable (Fig. S3, Supplementary Information) suggesting a similar probability for $^\bullet$OH attack on these carbons. This is further confirmed by the calculation of electronic energies and HOMO-LUMO energy gaps, and Gibbs free energy for both isomers. All quantities yielded similar results (Table S3, Supplementary Information) indicting that **P2** and **P2'** are likely formed in equivalent proportions.

The relative abundance of **P1**, (**P2 + P2'**), **P3**, and **P4** over time is shown in Fig. 13(g). The data reveal an initial increase in product formation, peaking at around 10 minutes, followed by a gradual decline and stabilisation at a plateau starting at around 15 minutes. This plateau is most pronounced for **P1** and **P2** + **P2'**, indicating the cessation of oxidation reactions leading to these products, likely due to competitive reactions. The relative abundance data show that **P1** was produced in the highest yield, followed by **P2** + **P2'**, and then **P3** and **P4** (Fig. 13(g)). Other studies on MB oxidation have also identified the formation of **P1**, **P2**, and **P3**, commonly known as Azure B, Azure A, and Azure C, respectively [105, 111].

According to the Fukui function analysis, carbons C1 and C13 are also susceptible to $^{\bullet}$OH attack, leading to the formation of product **P5** (*m/z* 72) identified as N,N-dimethyl(oxo)methaniminium (Scheme 3, Fig. 13(f)). A transformation product with *m/z* 72 was also reported by Li et al. (2021) [50] at the end of MB degradation, following oxidative ring opening. However, they proposed a structure of butanal, which differs from **P5** in our study. According to our results shown in Fig. 13(g), the relative abundance of **P5** increases rapidly early in the reaction, suggesting that it results from an early attack of the MB molecule to form N,N-dimethyl(oxo)methaniminium ion. **P5** appears to be stable, with its concentration steadily increasing throughout the electrochemical oxidation process. However, its rate of formation slows down after about 10 minutes, indicating that while the formation of **P5** continued, the degradation of MB may have slowed due to competing reactions.

Other products identified include **P6** (*m/z* 316), which likely results from the addition of two hydroxyl groups to MB at carbons C3 and C11, and **P7** (*m/z* 268), (Fig. 13(g)), resulting from N-demethylation and hydrogen abstraction from the N-methyl group. However, the relative abundances of these compounds were too low to be significant (Fig. 13(g)). Overall, the combination of mass spectrometry and molecular simulations provided valuable insights into the distinct degradation pathways of methylene blue suggested in Fig. 13.

To further illustrate the proposed degradation mechanism and establish a quantitative structure-activity relationship (SAR), we correlated the experimentally observed degradation rate constants of the products with their calculated Fukui indices. The site-specific susceptibility to radical attack for products P1, P2, and P3 was quantified using condensed Fukui radical indices (f^0) derived from DFT calculations. For each product, the maximum radical susceptibility index (f^0_{max}) was selected as a molecular descriptor and compared with the experimentally determined pseudo-first-order degradation rate constants (k_{obs}). These k_{obs} values were obtained from the degradation stage of each product, which commenced at 10, 10, and 5 minutes for P1, P2, and P3, respectively (Fig. 13(g)). As shown in Fig. 13(h), a strong positive correlation (R^2=0.991) was observed between k_{obs} and f^0_{max}. This finding indicates that radical attack at the most f^0-active atomic site (i.e., the site with the highest f^0 value) plays a dominant role in governing the electrochemical degradation kinetics. These results support a SAR in which hydroxyl radicals preferentially attack these high- f^0 sites, leading to faster degradation rates [112].

4. Conclusions

In summary, all electrodes studied (Ti, NiATOTi, and NiATOTiPt) generated hydroxyl radicals, albeit at different rates, leading to dye degradation rates proportional to hydroxyl radical production rates. Characterisation of the electrodes confirmed the coating of the titanium mesh with catalysts, though the uniformity of the coating was notably better for NiATOTiPt compared with NiATOTi due to the addition of Pt. Overall, NiATOTiPt outperformed the other electrodes in terms of hydroxyl radical production, degradation rates, and energy efficiency for the oxidation of methylene blue. The degradation rate constant, k, of NiATOTiPt was 2.6 and 1.3 times higher than NiATOTi and Ti at 5 V, and 7.5 and 3.3 times higher at 10 V, respectively. The degradation rates were found to increase as the circulation flow rate increased indicating that mass transfer could be a limiting factor of the process. However, higher flow rates caused flow channelling, reducing the overall efficiency of the electrochemical cell. Repeated use of the NiATOTiPt electrode did not result in any significant loss of performance. When applied to the treatment of simulated synthetic textile wastewater, the electrode exhibited higher degradation kinetics than those observed for MB in deionised water, albeit at the expense of increased electrical energy consumption (EEO). Although ozone production was found negligible, LC-MS/MS analysis confirmed that hydroxyl radicals were primarily responsible for dye degradation. The study also demonstrated that Fukui functions and density functional theory (DFT) provide valuable insights into the degradation pathway of methylene blue by hydroxyl radicals. In particular, the maximum Fukui function f^0 value showed a strong linear correlation with the experimental pseudo-first-order product degradation rate constants, indicating that compounds with higher local f^0 are degraded faster. Overall, this study highlights the effectiveness of anodic oxidation for the removal of contaminants in water. To support its practical implementation, upscaling the process and evaluating its performance under real industrial conditions are critical next steps, as they will help assess the technology's robustness, cost-effectiveness, and adaptability to complex contaminant profiles typically found in industrial and municipal effluents.

Acknowledgements

The authors acknowledge financial support by the award of a Royal Society Newton International Fellowship to N. Y. (Project No. NIF\R1\222187). SY was funded by a Schoalrship provided by Dwr Cymru (Welsh Water). IPT was funded by the Commonwealth Scholarship Commission and the Foreign, Commonwealth and Development Office in the UK. The authors would like to acknowledge the assistance provided by Swansea University Faculty of Science and Engineering AIM Facility, which was funded in part by the EPSRC (EP/M028267/1), the European Regional Development Fund through the Welsh Government (80708). All views expressed here are those of the authors, not the funding bodies.

Compliance with ethical standards

Conflict of interest: The authors declare that they have no conflict of interest.

CRediT author statement

NY: Data curation, Formal analysis, Funding acquisition, Investigation, Methodology, Visualization, Writing - Original Draft; **SY:** Data curation, Formal analysis, Investigation, Methodology, Writing - Original Draft; **IPT:** Data curation, Formal analysis, Investigation, Methodology, Writing - Original Draft; **REP:** Conceptualization, Funding acquisition, Project administration, Resources, Supervision, Writing - Review & Editing; **CT:** Conceptualization, Formal analysis, Funding acquisition, Methodology, Resources, Supervision, Visualization, Writing - Review & Editing.

References

[1] X. Teng, J. Li, Z. Wang, Z. Wei, C. Chen, K. Du, C. Zhao, G. Yang, Y. Li, Performance and mechanism of methylene blue degradation by an electrochemical process, RSC Adv, 10 (2020) 24712-24720.

[2] X. Zhang, J. Wang, X.X. Dong, Y.K. Lv, Functionalized metal-organic frameworks for photocatalytic degradation of organic pollutants in environment, Chemosphere, 242 (2020) 125144.

[3] C.R. Holkar, A.J. Jadhav, D.V. Pinjari, N.M. Mahamuni, A.B. Pandit, A critical review on textile wastewater treatments: Possible approaches, J Environ Manage, 182 (2016) 351-366.

[4] UNESCO World Water Assessment Programme, The United Nations World Water Development Report 2024: water for prosperity and peace. Available at: https://unesdoc.unesco.org/ark:/48223/pf0000388948, (2024).

[5] K. Yang, Y.Y. Liu, J.L. Qiao, Electrodeposition preparation of Ce-doped Ti/SnO_2-Sb electrodes by using selected addition agents for efficient electrocatalytic oxidation of methylene blue in water, Separation and Purification Technology, 189 (2017) 459-466.

[6] E.O. Nwanebu, X.C. Liu, E. Pajootan, V. Yargeau, S. Omanovic, Electrochemical Degradation of Methylene Blue Using a Ni-Co-Oxide Anode, Catalysts, 11 (2021) 793.

[7] V.S. Munagapati, H.Y. Wen, J.C. Wen, A.R.K. Gollakota, C.M. Shu, G.M. Reddy, Characterization of protonated amine modified lotus (*Nelumbo nucifera)* stem powder and its application in the removal of textile (Reactive Red 120) dye from liquid phase, Journal of Molecular Liquids, 338 (2021) 116486.

[8] R. Al-Tohamy, S.S. Ali, F. Li, K.M. Okasha, Y.A.G. Mahmoud, T. Elsamahy, H. Jiao, Y. Fu, J. Sun, A critical review on the treatment of dye-containing wastewater: Ecotoxicological and health concerns of textile dyes and possible remediation approaches for environmental safety, Ecotoxicology and Environmental Safety, 231 (2022) 113160.

[9] D.N. Saloumeh Ghasemian, Sasha Omanovic, and Viviane Yargeau, Photoelectrocatalytic degradation of pharmaceutical carbamazepine using Sb-doped Sn80%-W20%-oxide electrodes, Separation and Purification Technology, 188 (2017) 52-59.

[10] M. Li, C.P. Feng, Z.Y. Zhang, N. Sugiura, Efficient electrochemical reduction of nitrate to nitrogen using Ti/IrO_2-Pt anode and different cathodes, Electrochimica Acta, 54 (2009) 4600-4606.

[11] C.A. Martínez-Huitle, M.A. Rodrigo, I. Sirés, O. Scialdone, A critical review on latest innovations and future challenges of electrochemical technology for the abatement of organics in water, Applied Catalysis B: Environmental, 328 (2023) 122430.

[12] F. Long, D. Ghani, R. Huang, C. Zhao, Versatile electrode materials applied in the electrochemical advanced oxidation processes for wastewater treatment: A systematic review, Separation and Purification Technology, 354 (2025) 128725.

[13] L.M. Rifici, D.S. Cherry, J.L. Farris, J. Cairns, Jr., Acute and subchronic toxicity of methylene blue to larval fathead minnows (Pimephales promelas): Implications for aquatic toxicity testing, Environmental Toxicology and Chemistry, 15 (1996) 1304-1308.

[14] S. Li, Y. Cui, M. Wen, G. Ji, Toxic Effects of Methylene Blue on the Growth, Reproduction and Physiology of Daphnia magna, Toxics, 11 (2023).

[15] X. Zhang, Y. Hui, C. Fang, Y. Wang, F. Han, X. Lou, E.K. Fodjo, Y. Cai, C. Kong, Determination of Methylene Blue and Its Metabolite Residues in Aquatic Products by High-Performance Liquid Chromatography-Tandem Mass Spectrometry, Molecules, 26 (2021).

[16] D. Knozowski, M. Gmurek, Non-active anodes based on boron-doped diamond, PbO2 and SnO2-Sb for anodic oxidation of water contaminants: Synthesis, properties, and recent advances, Desalination and Water Treatment, 320 (2024) 100655.

[17] I. Messias, J. Kupferberg, A.R. Bielinski, R. Nagao, A.B.F. Martinson, P. Papa Lopes, Quantification of Reactive Oxygen Species Produced from Electrocatalytic Materials, ACS Catalysis, (2025) 2750-2759.

[18] L. Huang, J. Zhang, G. Wang, D. Wang, Z. Li, S. Zhou, X. Di, X. Feng, Experimental treatment of pickled vegetable wastewater by electrofenton method based on modified PbO2 electrode, Process Safety and Environmental Protection, 193 (2025) 514-532.

[19] O. Ganzenko, D. Huguenot, E.D. van Hullebusch, G. Esposito, M.A. Oturan, Electrochemical advanced oxidation and biological processes for wastewater treatment: a review of the combined approaches, Environmental Science and Pollution Research, 21 (2014) 8493-8524.

[20] O. Scialdone, Electrochemical oxidation of organic pollutants in water at metal oxide electrodes: A simple theoretical model including direct and indirect oxidation processes at the anodic surface, Electrochimica Acta, 54 (2009) 6140-6147.

[21] A.M. Polcaro, A. Vacca, S. Palmas, M. Mascia, Electrochemical treatment of wastewater containing phenolic compounds: oxidation at boron-doped diamond electrodes, Journal of Applied Electrochemistry, 33 (2003) 885-892.

[22] D. Chu, M. Xu, J. Lu, P. Zheng, G. Qin, X. Yuan, Electrocatalytic reduction of diethyl oximinomalonate at a Ti/nanoporous TiO electrode, Electrochemistry Communications, 10 (2008) 350-353.

[23] P. Cañizares, M. Díaz, J.A. Domínguez, J. García-Gómez, M.A. Rodrigo, Electrochemical oxidation of aqueous phenol wastes on synthetic diamond thin-film electrodes, Industrial & Engineering Chemistry Research, 41 (2002) 4187-4194.

[24] X. Qian, K. Peng, L. Xu, S. Tang, W. Wang, M. Zhang, J. Niu, Electrochemical decomposition of PPCPs on hydrophobic Ti/SnO2-Sb/La-PbO2 anodes: Relationship between surface hydrophobicity and decomposition performance, Chemical Engineering Journal, 429 (2022) 132309.

[25] A. Saurabh, C.M. Meghana, P.K. Singh, P.C. Verma, Titanium-based materials: synthesis, properties, and applications, Materials Today: Proceedings, 56 (2022) 412-419.

[26] S. Geiger, O. Kasian, A.M. Mingers, K.J.J. Mayrhofer, S. Cherevko, Stability limits of tin-based electrocatalyst supports, Sci Rep, 7 (2017) 4595.

[27] Q. Bi, W. Guan, Y. Gao, Y.-r. Cui, S. Ma, J.-q. Xue, Study of the mechanisms underlying the effects of composite intermediate layers on the performance of Ti/SnO2-Sb-La electrodes, Electrochimica Acta, (2019).

[28] C. Shao, F. Zhang, X. Li, J. Zhang, Y. Jiang, H. Cheng, K. Zhu, Influence of Cr doping on the oxygen evolution potential of SnO2/Ti and Sb-SnO2/Ti electrodes, Journal of Electroanalytical Chemistry, 832 (2019) 436-443.

[29] Y. Li, H. Ma, Q. Li, G. Yan, S. Guo, One-step synthesis of Pt-Nd co-doped Ti/SnO2-Sb nanosphere electrodes used to degrade nitrobenzene, Environmental Science and Pollution Research, 31 (2024) 4528-4538.

[30] H. Zhang, J. Qian, J. Zhang, J. Xu, Enhancing the electrochemical activity and stability of Sb-SnO2 based electrodes by the introduction of nickel oxide, Journal of Alloys and Compounds, 882 (2021) 160700.

[31] D. Lim, Y. Kim, D. Nam, S. Hwang, S.E. Shim, S.-H. Baeck, Influence of the Sb content in Ti/SnO2-Sb electrodes on the electrocatalytic behaviour for the degradation of organic matter, Journal of Cleaner Production, 197 (2018) 1268-1274.

[32] J. Zhang, M. Yang, X. Zhu, J. Dang, J. Ma, B. Liu, T. Huang, M. Ouyang, F. Yang, The role of Pt doping on electrochemical performance and cost of alkaline water electrolysis catalysts, Chemical Engineering Journal, 476 (2023) 146576.

[33] C. Jeong, T.H. Kim, K.-W. Lee, T.S. Lee, Efficient, electrochemical degradation of organic pollutants via nanofibrous Pt/Ir–RuO2 electrode with enhanced stability, Chemosphere, 369 (2024) 143826.

[34] S.-F. Kang, C.-H. Liao, M.-C. Chen, Pre-oxidation and coagulation of textile wastewater by the Fenton process, Chemosphere, 46 (2002) 923-928.

[35] I.A. Alaton, I.A. Balcioglu, D.W. Bahnemann, Advanced oxidation of a reactive dyebath effluent: comparison of O3, H2O2/UV-C and TiO2/UV-A processes, Water Research, 36 (2002) 1143-1154.

[36] J.R. Bolton, K.G. Bircher, W. Tumas, C.A. Tolman, Figures-of-merit for the technical development and application of advanced oxidation technologies for both electric- and solar-driven systems - (IUPAC Technical Report), Pure Appl Chem, 73 (2001) 627-637.

[37] M.J.T. Frisch, G. W.; Schlegel, H. B.; Scuseria, G. E.;Robb, M. A.; Cheeseman, J. R.; Scalmani, G.; Barone, V.; Petersson,G. A.; Nakatsuji, H. et al. , . Gaussian 16, Revision C.01; , 2016.

[38] a.F.-W.C. Tian Lu, Comparison of computational methods for atomic charges, Acta Physico-Chimica Sinica, 28 (2012) 1-18.

[39] a.F.C. Tian Lu, Multiwfn: A multifunctional wavefunction analyzer, Journal of computational chemistry, 33 (2012) 580-592.

[40] a.Q.C. Tian Lu, mwfn: A strict, concise and extensible format for electronic wavefunction storage and exchange, ChemRxiv, (2021).

[41] Y.J. Feng, Y.H. Cui, B. Logan, Z.Q. Liu, Performance of Gd-doped Ti-based Sb-SnO_2 anodes for electrochemical destruction of phenol, Chemosphere, 70 (2008) 1629-1636.

[42] R.R.Y. Navneet Yadav, and Kajal Kumar Dey, Microwave assisted formation of trimetallic AuPtCu nanoparticles from bimetallic nano-islands: why it is a superior new age biocidal agent compared to monometallic & bimetallic nanoparticles, Journal of Alloys and Compounds, 896 (2022) 163073.

[43] A.K. Verma, R.R. Yadav, N. Yadav, S.P. Singh, K.K. Dey, D. Singh, Study of Ultrasonic Attenuation and Thermal Conduction in Bimetallic Gold/ Platinum Nanofluids Effect of

thermal conductivity on ultrasonic attenuation of gold and gold/ platinum nanofluids, Johnson Matthey Technology Review, 65 (2021) 556-567.

[44] A.K.J. Navneet Yadav, K.K. Dey, V. B. Yadav, G. Nath, A.K. Srivastava, and R.R. Yadav, Trimetallic Au/Pt/Ag based nanofluids for enhanced antibacterial applications, Materials Chemistry and Physics, 218 (2018) 10–17.

[45] D.R.J. S. P. Du Preez, M. E. A. Warwick, A. Falch, P. T. Sekoai, C. Mota das Neves Quaresma, D. G. Bessarabov, and C. W. Dunnill., Thermally stable Pt/Ti mesh catalyst for catalytic hydrogen combustion, International Journal of Hydrogen Energy, 45 (2020) 16851-16864.

[46] X.Y. Zhang, D. Li, J.F. Wan, X.J. Yu, Hydrothermal synthesis of TiO nanosheets photoelectrocatalyst on Ti mesh for degradation of norfloxacin: Influence of pickling agents, Materials Science in Semiconductor Processing, 43 (2016) 47-54.

[47] C.M. Lees, J.L. Lansing, S.L. Morelly, S.E. Lee, M.H. Tang, Ni- and Sb-Doped SnO2 Electrocatalysts with High Current Efficiency for Ozone Production via Electrodeposited Nanostructures, Journal of The Electrochemical Society, 165 (2018) E833-E840.

[48] M.M.E. Duarte, A.S. Pilla, J.M. Sieben, C.E. Mayer, Platinum particles electrodeposition on carbon substrates, Electrochemistry Communications, 8 (2006) 159-164.

[49] L. Huang, D. Li, J. Liu, L. Yang, C. Dai, N. Ren, Y. Feng, Construction of TiO(2) nanotube clusters on Ti mesh for immobilizing Sb-SnO(2) to boost electrocatalytic phenol degradation, J Hazard Mater, 393 (2020) 122329.

[50] G.Y. Li, G.Y. Zeng, Z.K. Chen, J.M. Hong, X.D. Ji, Z.Q. Lan, X.F. Tan, M.F. Li, X.J. Hu, C.F. Tang, In Situ Coupling Carbon Defective C_3N_5 Nanosheet with Ag_2CO_3 for Effective Degradation of Methylene Blue and Tetracycline Hydrochloride, Nanomaterials, 12 (2022) 2701.

[51] T.M. Koo, H.E. Fu, J.H. Moon, E. Oh, Y. Kim, M.J. Ko, Y.K. Kim, Porous Iron Oxide Core-Gold Satellite Nanocomposite: A Cost-Effective and Recyclable Solution for Photocatalytic Wastewater Treatment, Small Sci, 4 (2024) 2300266.

[52] M. Zimbone, G. Cacciato, L. Spitaleri, R.G. Egdell, M.G. Grimaldi, A. Gulino, Sb-Doped Titanium Oxide: A Rationale for Its Photocatalytic Activity for Environmental Remediation, Acs Omega, 3 (2018) 11270-11277.

[53] X. Zhou, S.R. Yu, J. Wang, J. Zang, Z.X. Lv, Superhydrophilic anti-corrosive and superhydrophobic durable TiO_2/Ti mesh for oil/water separation, Journal of the Taiwan Institute of Chemical Engineers, 105 (2019) 124-133.

[54] J. Yue, A.J. Epstein, Xps Study of Self-Doped Conducting Polyaniline and Parent Systems, Macromolecules, 24 (1991) 4441-4445.

[55] X. Li, C.R. Shao, J.G. Yu, K.G. Zhu, Preparation and Investigation of Nickel-Antimony co-doped Tin Oxide Anodes for Electro-catalytic Oxidation of Organic Pollutions, International Journal of Electrochemical Science, 14 (2019) 205-218.

[56] a.F.B.L. X. Z. Li, Surface characterization and photocatalytic reactivity of innovative Ti/TiO 2 and Ti/Pt− TiO 2 mesh photoelectrodes, Journal of applied electrochemistry, 32 (2002) 203-210.

[57] J. Yadav, M. Rani, T.C. Zhang, U. Shanker, Efficient photo-adsorptive eradication of endocrine disrupting pesticides by chitosan co- decorated metal oxide bio-nanocomposite, Environmental Science and Pollution Research, 30 (2023) 72523-72538.

[58] Keshu, M. Rani, U. Shanker, One pot green synthesis of Al doped zinc ferrite nanoparticle decorated with reduced graphene oxide for photocatalytic remediation of organic pollutants: Green synthesis, kinetics, and photoactivity, Chemosphere, 344 (2023) 140381.

[59] M.A.-F. Adrián Barroso-Bogeat, Carmen Fernández-González, Antonio Macías-García, and Vicente Gómez-Serrano, Preparation of activated carbon-SnO2, TiO2, and WO3 catalysts. Study by FT-IR spectroscopy, Industrial & Engineering Chemistry Research, 55 (2016) 5200-5206.

[60] P. Saikia, P. Borah, D. Borah, D. Gogoi, J. Rout, N.N. Ghosh, C.R. Bhattacharjee, Facile green synthesis of rGO and NiO, and fabrication of a novel ternary nanoheterostructure NiO@g-C3N4-rGO as earth abundant superior photocatalyst for dye degradation, Materials Today Sustainability, 24 (2023) 100595.

[61] D.J.J. Lidija V. Trandafilović, X. Zhang, S. Ptasińska, and M. D. Dramićanin, Enhanced photocatalytic degradation of methylene blue and methyl orange by ZnO: Eu nanoparticles, Applied Catalysis B: Environmental, 203 (2017) 740-752.

[62] A.K. Singh, N. Shukla, D.K. Verma, Kavita, B. Kumar, R.B. Rastogi, Enhancement of Triboactivity of Nanolamellar Graphitic-C_3N_4 by N-Doped ZnO Nanorods, Industrial & Engineering Chemistry Research, 60 (2021) 864-874.

[63] Z.Y. Hu, C. Guo, P. Wang, R. Guo, X.W. Liu, Y. Tian, Electrochemical degradation of methylene blue by Pb modified porous SnO2 anode, Chemosphere, 305 (2022) 135447.

[64] Y. Son, V. Mishin, W. Welsh, S.E. Lu, J.D. Laskin, H. Kipen, Q.M. Meng, A Novel High-Throughput Approach to Measure Hydroxyl Radicals Induced by Airborne Particulate Matter, International Journal of Environmental Research and Public Health, 12 (2015) 13678-13695.

[65] G.X. Castillo-Cabrera, C.I. Pliego-Cerdán, E. Méndez, P.J. Espinoza-Montero, Step-by-step guide for electrochemical generation of highly oxidizing reactive species on BDD for beginners, Front Chem, 11 (2024) 1298630.

[66] S.O. Ganiyu, C.A. Martínez-Huitle, M.A. Oturan, Electrochemical advanced oxidation processes for wastewater treatment: Advances in formation and detection of reactive species and mechanisms, Current Opinion in Electrochemistry, 27 (2021) 100678.

[67] X. Li, H. Xu, W. Yan, Fabrication and Characterization of a PbO2-TiN Composite Electrode by Co-Deposition Method, Journal of The Electrochemical Society, 163 (2016) D592.

[68] R. Jaimes-López, A. Jiménez-Vázquez, S. Pérez-Rodríguez, L.A. Estudillo-Wong, N. Alonso-Vante, Catalyst for the Generation of OH Radicals in Advanced Electrochemical Oxidation Processes: Present and Future Perspectives, Catalysts, 14 (2024) 703.

[69] J. Nobbs, C. Tizaoui, A Modified Indigo Method for the Determination of Ozone in Nonaqueous Solvents, Ozone: Science & Engineering, 36 (2014) 110-120.

[70] H. Bader, J. Hoigné, Determination of ozone in water by the indigo method, Water Research, 15 (1981) 449-456.

[71] S. Sandin, A. Abo Hamad, M. Cuartero, R. de Marco, G.A. Crespo, J. Bäckström, A. Cornell, Deactivation and selectivity for electrochemical ozone production at Ni- and Sb-doped SnO2 / Ti electrodes, Electrochimica Acta, 335 (2020) 135645.

[72] S. Kim, S.K. Choi, B.Y. Yoon, S.K. Lim, H. Park, Effects of electrolyte on the electrocatalytic activities of RuO2/Ti and Sb–SnO2/Ti anodes for water treatment, Applied Catalysis B: Environmental, 97 (2010) 135-141.

[73] G. de O S Santos, V.M. Vasconcelos, R.S. da Silva, M.A. Rodrigo, K.I.B. Eguiluz, G.R. Salazar-Banda, New laser-based method for the synthesis of stable and active Ti/SnO2–Sb anodes, Electrochimica Acta, 332 (2020) 135478.

[74] H. Xu, A.-P. Li, Q. Qi, W. Jiang, Y.-M. Sun, Electrochemical degradation of phenol on the La and Ru doped Ti/SnO2-Sb electrodes, Korean Journal of Chemical Engineering, 29 (2012) 1178-1186.

[75] Y.-J.F. Yu-Hong Cui, and Zheng-Qian Liu, Influence of rare earths doping on the structure and electro-catalytic performance of Ti/Sb–SnO2 electrodes, Electrochimica Acta, 54 (2009) 4903-4909.

[76] A.I. del Río, J. Fernández, J. Molina, J. Bonastre, F. Cases, On the behaviour of doped SnO2 anodes stabilized with platinum in the electrochemical degradation of reactive dyes, Electrochimica Acta, 55 (2010) 7282-7289.

[77] F. Qiu, L. Wang, Y. Fan, Y. Pan, H. Song, Z. Ye, S. Zhang, Review on Structural Adjustment Strategies of Titanium-Based Metal Oxide Dimensionally Stable Anodes in Electrochemical Advanced Oxidation Technology, Advanced Engineering Materials, 26 (2024).

[78] D.B. Miklos, C. Remy, M. Jekel, K.G. Linden, J.E. Drewes, U. Hübner, Evaluation of advanced oxidation processes for water and wastewater treatment - A critical review, Water Res, 139 (2018) 118-131.

[79] L. Xu, X. Cui, J. Liao, Y. Liu, B. Jiang, J. Niu, Synchronous mineralization of three aqueous non-steroidal anti-inflammatory drugs in electrochemical advanced oxidation process, Chinese Chemical Letters, 33 (2022) 3701-3704.

[80] Y. Zhang, K. Shaad, D. Vollmer, C. Ma, Treatment of Textile Wastewater Using Advanced Oxidation Processes—A Critical Review, Water, 13 (2021) 3515.

[81] M. Lanzarini-Lopes, S. Garcia-Segura, K. Hristovski, P. Westerhoff, Electrical energy per order and current efficiency for electrochemical oxidation of p-chlorobenzoic acid with boron-doped diamond anode, Chemosphere, 188 (2017) 304-311.

[82] W. Yang, Z. Deng, Y. Wang, L. Ma, K. Zhou, L. Liu, Q. Wei, Porous boron-doped diamond for efficient electrocatalytic elimination of azo dye Orange G, Separation and Purification Technology, 293 (2022) 121100.

[83] B. Vahid, A. Khataee, Photoassisted electrochemical recirculation system with boron-doped diamond anode and carbon nanotubes containing cathode for degradation of a model azo dye, Electrochimica Acta, 88 (2013) 614-620.

[84] M.H. Zhou, H. Särkkä, M. Sillanpää, A comparative experimental study on methyl orange degradation by electrochemical oxidation on BDD and MMO electrodes, Separation and Purification Technology, 78 (2011) 290-297.

[85] C.A.A. Martínez-Huitle, M.A. Rodrigo, I. Sirés, O. Scialdone, Single and Coupled Electrochemical Processes and Reactors for the Abatement of Organic Water Pollutants: A Critical Review, Chemical reviews, 115 24 (2015) 13362-13407.

[86] E.O. Nwanebu, X. Liu, E. Pajootan, V. Yargeau, S. Omanovic, Electrochemical Degradation of Methylene Blue Using a Ni-Co-Oxide Anode, Catalysts, 11 (2021) 793.

[87] R. Stirling, W.S. Walker, P. Westerhoff, S. Garcia-Segura, Techno-economic analysis to identify key innovations required for electrochemical oxidation as point-of-use treatment systems, Electrochimica Acta, 338 (2020) 135874.

[88] J. Radjenovic, D.L. Sedlak, Challenges and Opportunities for Electrochemical Processes as Next-Generation Technologies for the Treatment of Contaminated Water, Environmental Science & Technology, 49 (2015) 11292-11302.

[89] A. Alaoui, K. El Kacemi, K. El Ass, S. Kitane, S. El Bouzidi, Activity of Pt/MnO2 electrode in the electrochemical degradation of methylene blue in aqueous solution, Separation and Purification Technology, 154 (2015) 281-289.

[90] M.A.E.H. Hassan, M.M.E. Jamal, Kinetic Study of the Electrochemical Oxidation of Methylene Blue with Pt Electrode, Portugaliae Electrochimica Acta, 30 (2012) 351-359.

[91] S. Liu, Z. Wang, S. Qiu, F. Deng, Mechanism in pH effects of electrochemical reactions: a mini-review, Carbon Letters, 34 (2024) 1269-1286.

[92] Z.K. Yan Li, Lina Jia, Dan Zhang, Yan Hong, Jingjing Liu, Haibo Huang, Siqi Li & Song Liu, Elucidating the Role of Mass Transfer in Electrochemical Redox Reactions on Electrospun Fibers, Transactions of Tianjin University, 29 (2023) 313–320.

[93] L.F.A. Inmaculada García-López, Thomas Turek, Vicente Ismael Águeda and Amalio Garrido-Escudero, Mass transfer enhancement in electrochemical flow cells through 3D-printed biomimetic channels, Reaction Chemistry & Engineering, 8 (2023) 1776-1784.

[94] T.L. Xuefei Wang, Haitao Li, Chao Han, Panpan Su, Na Ta, San Ping Jiang, Biao Kong, Jian Liu and Zhenguo Huang*, Balancing Mass Transfer and Active Sites to Improve Electrocatalytic Oxygen Reduction by B,N Codoped C Nanoreactors, Nano Letters, 23 (2023) 4699-4707.

[95] F. Wang, W. Wu, Z. Lu, B. Yuan, Y. Zhao, T.L. Liu, Understanding impacts of flow rate on performance of desalination flow batteries, Materials Today Energy, 21 (2021) 100750.

[96] R. Pol, M. Guerrero, E. García-Lecina, A. Altube, E. Rossinyol, S. Garroni, M.D. Baró, J. Pons, J. Sort, E. Pellicer, Ni-, Pt- and (Ni/Pt)-doped TiO2 nanophotocatalysts: A smart approach for sustainable degradation of Rhodamine B dye, Applied Catalysis B: Environmental, 181 (2016) 270-278.

[97] N.H. Luan, Y.-T. Yang, C.-F. Chang, Electrochemical degradation of methylene blue accompanied with the reduction of CO2 by using carbon nanotubes grown on carbon fiber electrodes, Sustainable Environment Research, 32 (2022) 13.

[98] Y. Duan, Y. Chen, Q. Wen, T. Duan, Fabrication of dense spherical and rhombic Ti/Sb–SnO2 electrodes with enhanced electrochemical activity by colloidal electrodeposition, Journal of Electroanalytical Chemistry, 768 (2016) 81-88.

[99] T. Duan, Y. Chen, Q. Wen, Y. Duan, Enhanced electrocatalytic activity of nano-TiN composited Ti/Sb–SnO2 electrode fabricated by pulse electrodeposition for methylene blue decolorization, RSC Advances, 4 (2014) 57463-57475.

[100] DWI, Drinking Water Standards and Regulations. Available at: https://www.dwi.gov.uk/drinking-water-standards-and-regulations/.

[101] M. Panizza, G. Cerisola, Direct And Mediated Anodic Oxidation of Organic Pollutants, Chemical Reviews, 109 (2009) 6541-6569.

[102] M.A. Alkhadra, X. Su, M.E. Suss, H. Tian, E.N. Guyes, A.N. Shocron, K.M. Conforti, J.P. de Souza, N. Kim, M. Tedesco, K. Khoiruddin, I.G. Wenten, J.G. Santiago, T.A. Hatton, M.Z. Bazant, Electrochemical Methods for Water Purification, Ion Separations, and Energy Conversion, Chem Rev, 122 (2022) 13547-13635.

[103] C.A. Martínez-Huitle, E. Brillas, Decontamination of wastewaters containing synthetic organic dyes by electrochemical methods: A general review, Applied Catalysis B: Environmental, 87 (2009) 105-145.

[104] J.M. Small, H. Hintelmann, Methylene blue derivatization then LC-MS analysis for measurement of trace levels of sulfide in aquatic samples, Anal Bioanal Chem, 387 (2007) 2881-2886.

[105] M.A. Rauf, M.A. Meetani, A. Khaleel, A. Ahmed, Photocatalytic degradation of Methylene Blue using a mixed catalyst and product analysis by LC/MS., Chemical Engineering Journal 157 (2010) 373-378.

[106] S.G.Z.-S. Minju Lee, J. Samuel Arey, Kathrin Fenner, and Urs von Gunten, Development of prediction models for the reactivity of organic compounds with ozone in aqueous solution by quantum chemical calculations: the role of delocalized and localized molecular orbitals, Environmental science & technology, 49 (2015) 9925-9935.

[107] C. Von Sonntag, and Urs Von Gunten, Chemistry of ozone in water and wastewater treatment, IWA publishing, 2012.

[108] L.S.S. Ilza Dalmázio, Renata P. Lopes, Marcos N. Eberlin, and Rodinei Augusti, Advanced oxidation of caffeine in water: on-line and real-time monitoring by electrospray ionization mass spectrometry, Environmental science & technology, 39 (2005) 5982-5988.

[109] S.A.G.S. Pedro M.P. Santos, Gonçalo C. Justino, Abel J.S.C. Vieira, Demethylation of theophylline (1,3-dimethyl-xanthine) to 1-methylxanthine: the first stepof an antioxidising cascade, Redox Report, 15 (2010) 138-144.

[110] K.K. Chihiro Yogi, Noriyuki Wada, Hiroshi Tokumoto, Tomoo Takai, Tadashi Mizoguchi, and Hitoshi Tamiaki, Photocatalytic degradation of methylene blue by TiO2 film and Au particles-TiO2 composite film, Thin Solid Films, 516 (2008) 5881-5884.

[111] N. Martin, Y. Leprince-Wang, HPLC-MS and UV-Visible Coupled Analysis of Methylene Blue Photodegradation by Hydrothermally Grown ZnO Nanowires, Phys Status Solidi A, 218 (2021) 2100532.

[112] W. Ding, H. Chen, H. Ji, Efficiently Predicting Reaction Rates and Revealing Reactive Sites with a Molecular Image-Vision Transformer and Fukui Function Validation, Industrial & Engineering Chemistry Research, 63 (2024) 7064-7072.

Figure1

Figures

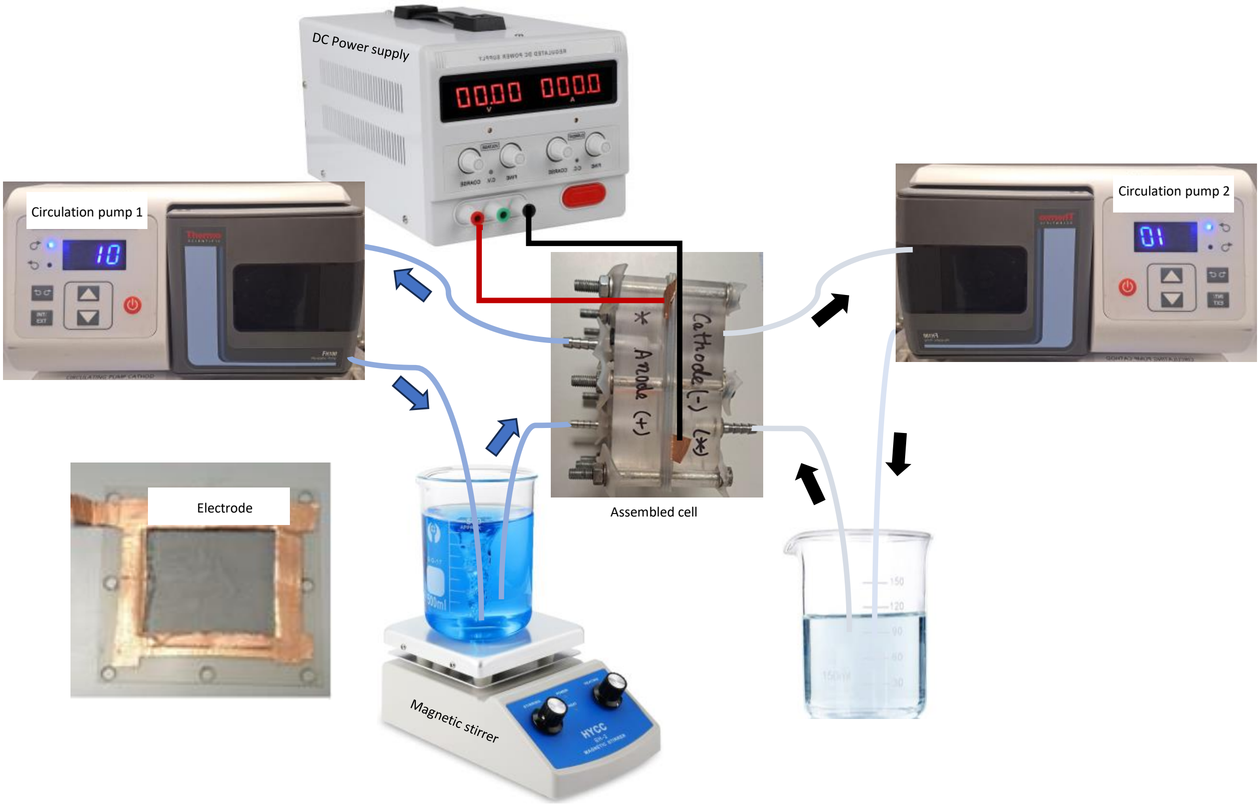

Fig. 1: Experimental set-up for electrochemical degradation of methylene blue

Figure2

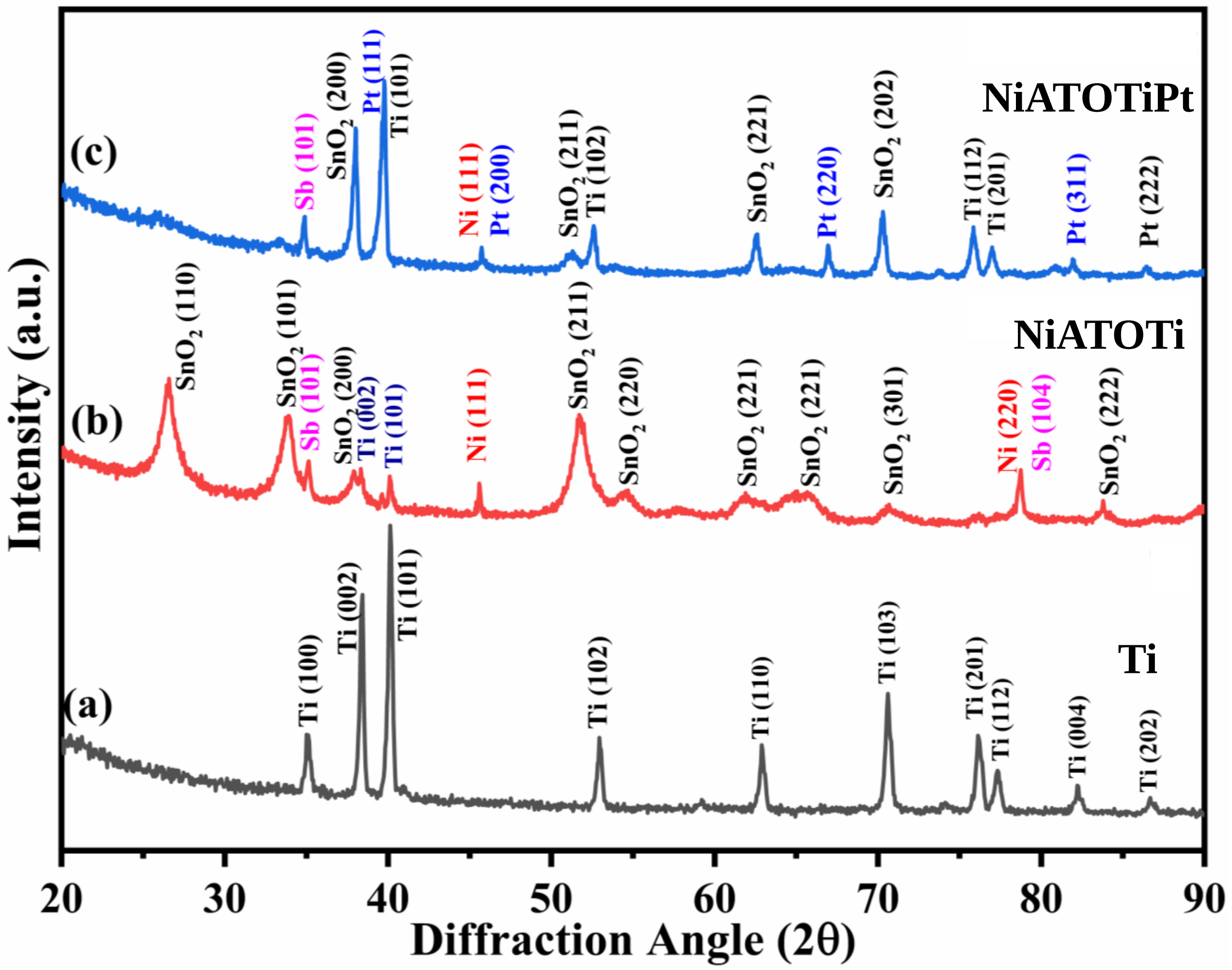

Fig. 2: XRD patterns of (a) Ti; (b) NiATOTi; and (c) NiATOTiPt electrodes

Figure3

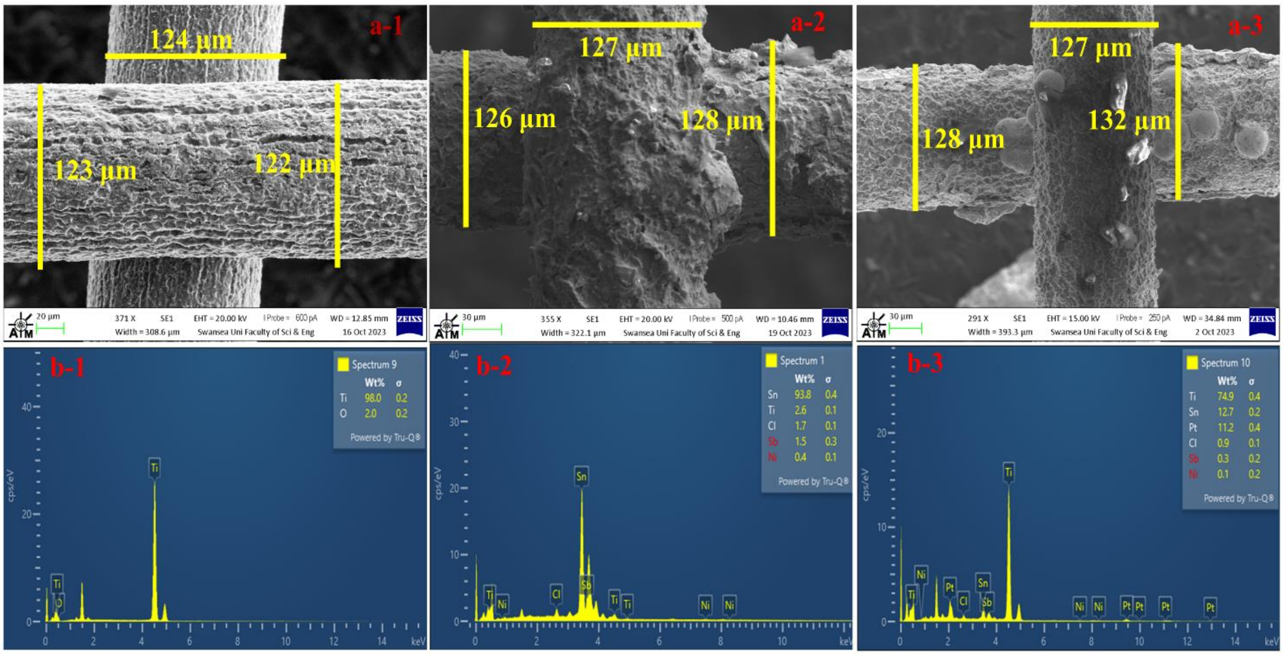

Fig. 3: SEM (a) and EDS (b) of Ti (1); NiATOTi (2); and NiATOTiPt (3) electrodes

Figure4

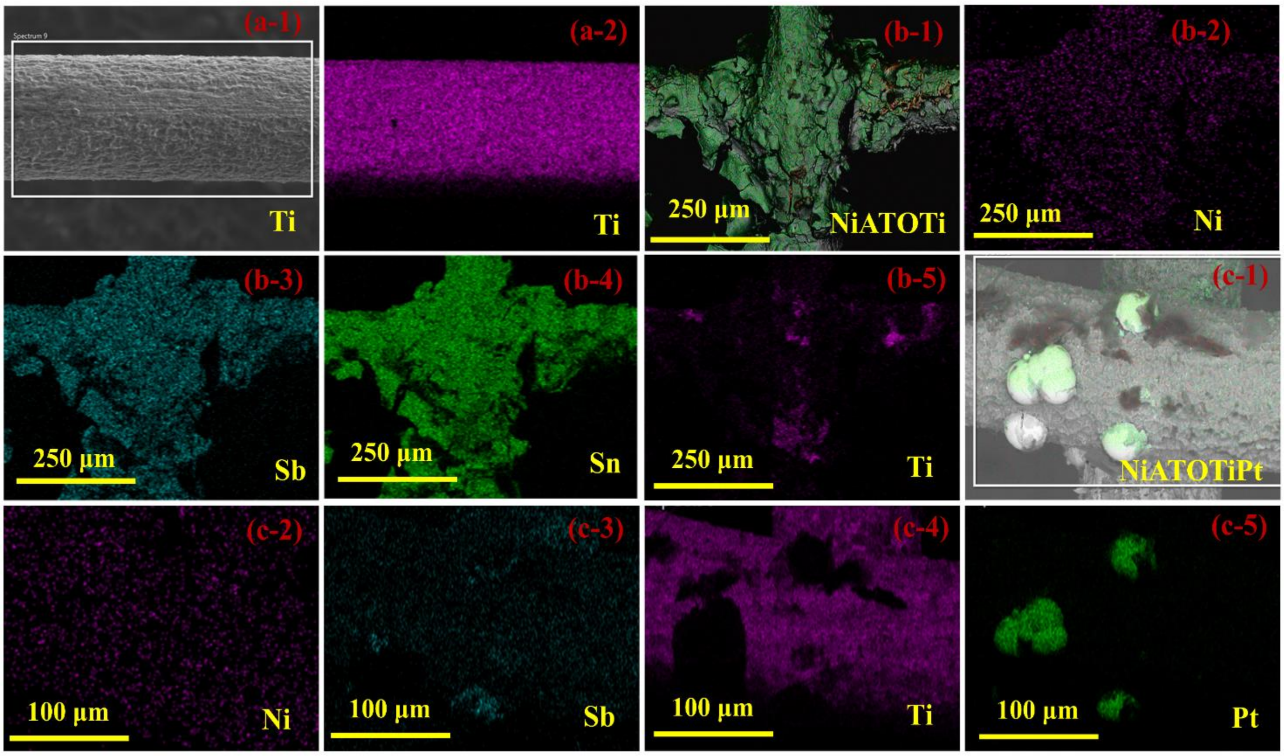

Fig. 4: Elemental mapping of (a) Ti; (b) NiATOTi; and (c) NiATOTiPt electrodes

Figure5

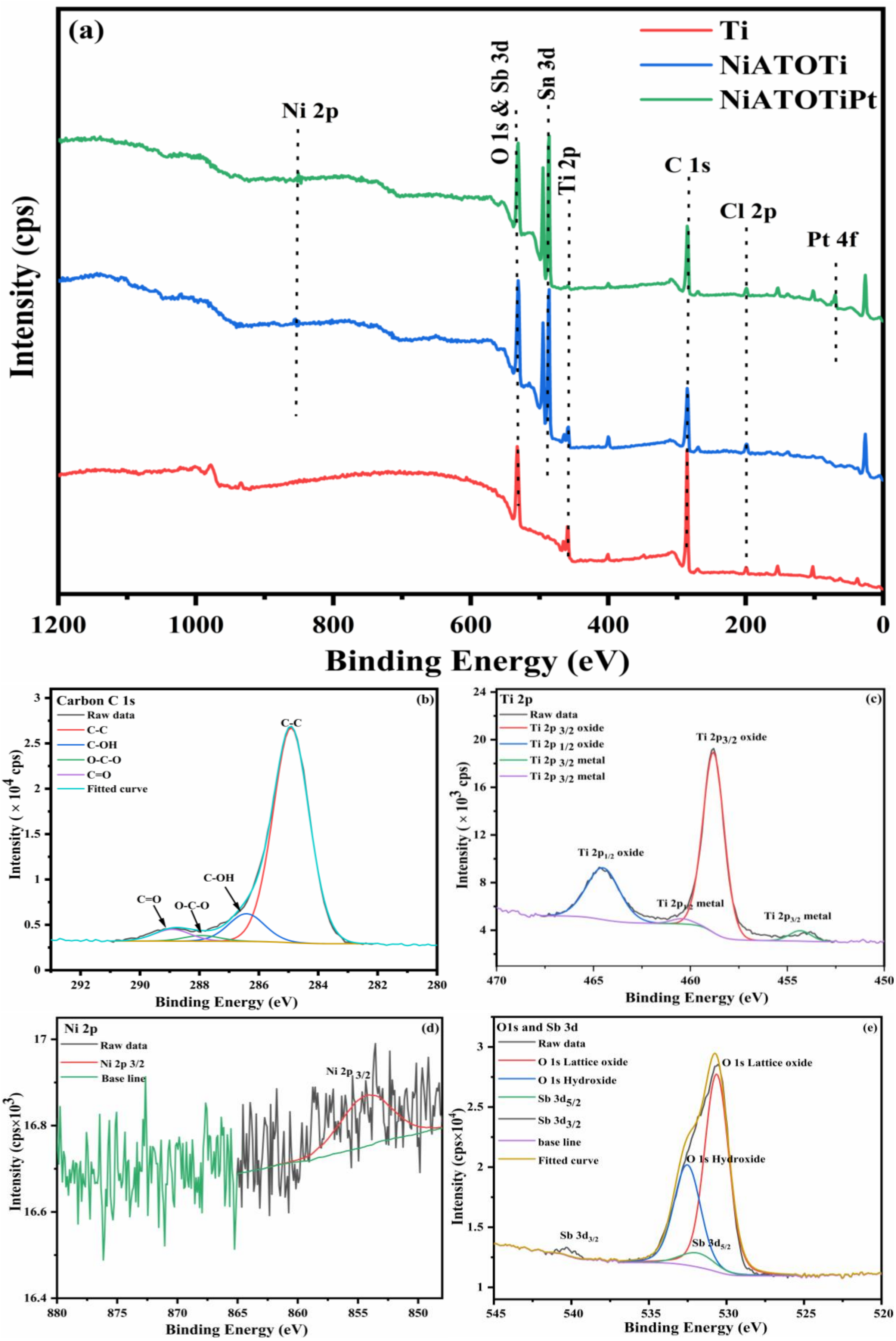
(a)
Ti
NiATOTi
NiATOTiPt
Ni 2p
O 1s & Sb 3d
Sn 3d
Ti 2p
C 1s
Cl 2p
Pt 4f
Intensity (cps)
1200
1000
800
600
400
200
0
Binding Energy (eV)
Carbon C 1s
(b)
Raw data
C-C
C-OH
O-C-O
C=O
Fitted curve
C-C
C-OH
C=O
O-C-O
Intensity (× 10^4 cps)
Binding Energy (eV)
Ti 2p
(c)
Raw data
Ti 2p 3/2 oxide
Ti 2p 1/2 oxide
Ti 2p 3/2 metal
Ti 2p 3/2 metal
Ti 2p3/2 oxide
Ti 2p1/2 oxide
Ti 2p3/2 metal
Ti 2p3/2 metal
Intensity (× 10^3 cps)
Binding Energy (eV)
Ni 2p
(d)
Raw data
Ni 2p 3/2
Base line
Ni 2p 3/2
Intensity (cps×10^3)
Binding Energy (eV)
O1s and Sb 3d
(e)
Raw data
O 1s Lattice oxide
O 1s Hydroxide
Sb 3d5/2
Sb 3d3/2
base line
Fitted curve
O 1s Lattice oxide
O 1s Hydroxide
Sb 3d3/2
Sb 3d5/2
Intensity (cps×10^4)
Binding Energy (eV)

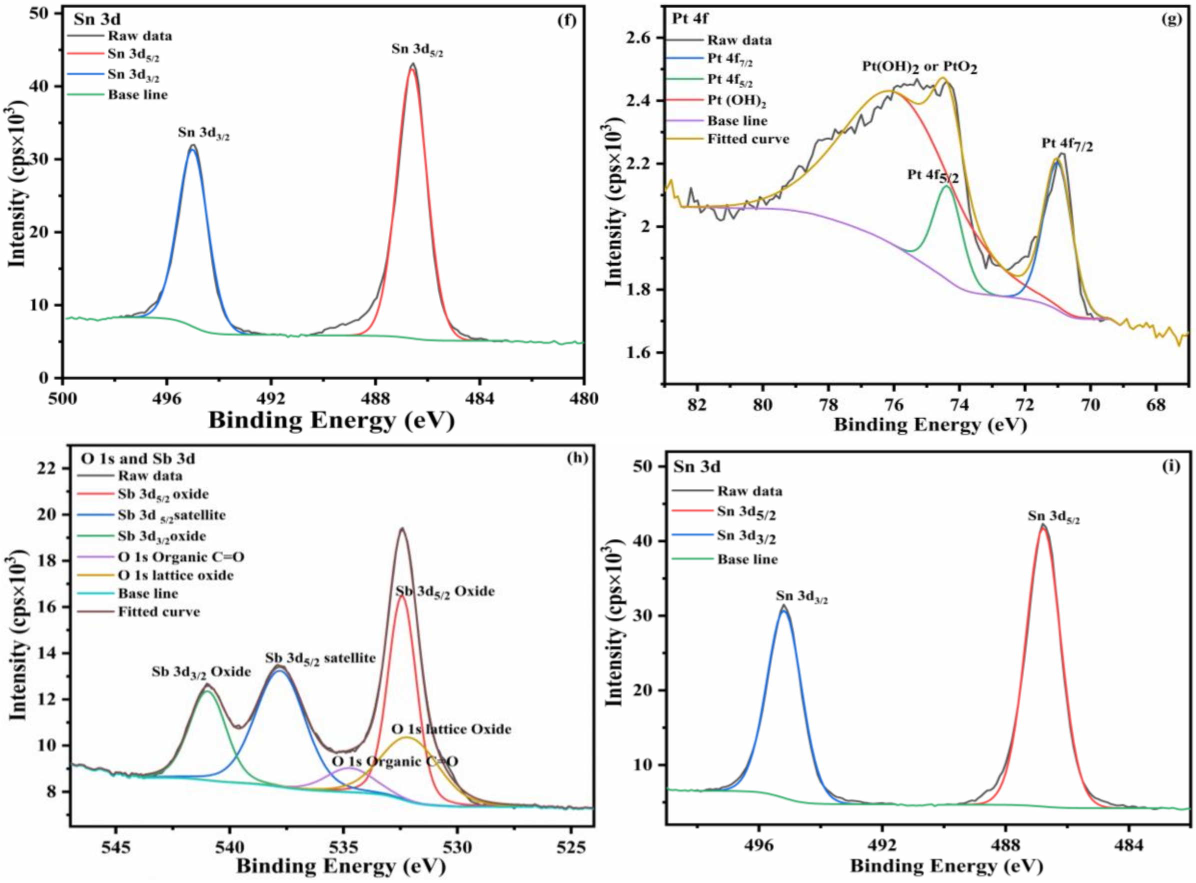

Fig. 5: (a) Wide scan spectrum of Ti, NiATOTi and NiATOTiPt electrodes; fitted curves of (b) C1s; (c) Ti 2p; (d) Ni 2p; (e) Sb 3d; (f) Sn 3d; (g) Pt 4f; (h) Sb 3d; and (i) Sn 3d

Figure6

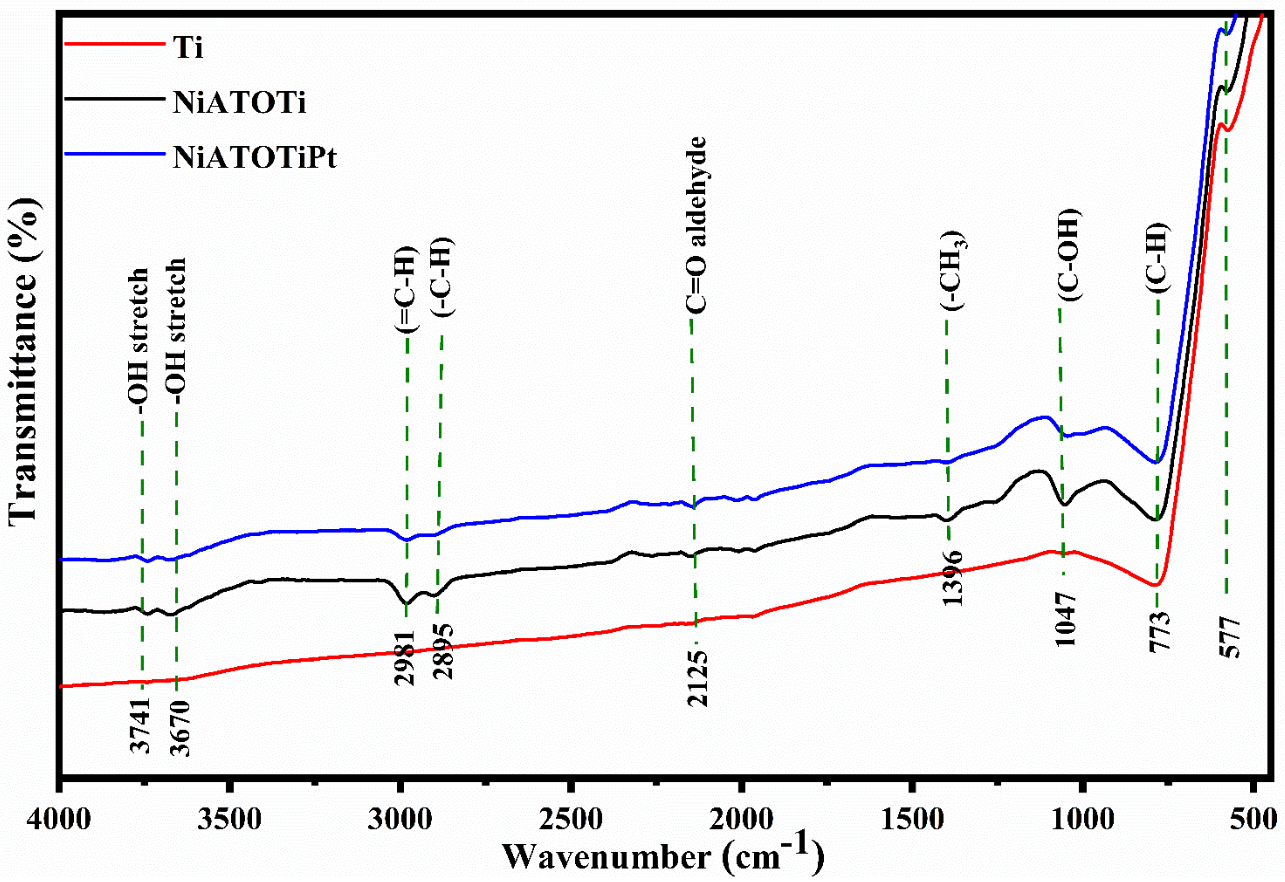

Fig. 6: FTIR spectra of Ti, NiATOTi, and NiATOTiPt electrodes following the degradation of MB solution.

Figure7

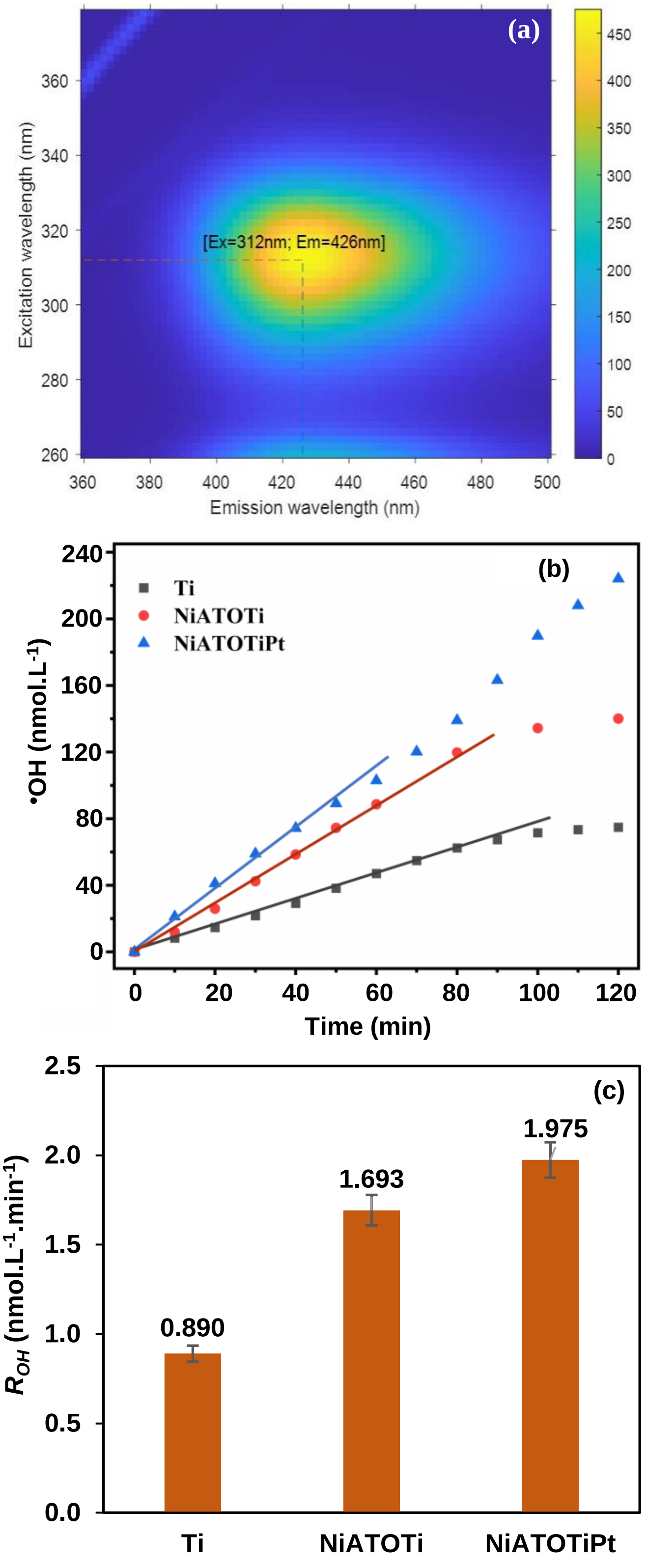

Fig. 7: (a) Excitation/Emission wavelengths for OHTPA fluorescence; (b) hydroxyl radical production versus time; (c) effect of electrode type on initial $^{\bullet}$OH production rate (Voltage = 5 V, flow rate= 88.5 mL/min)

Figure8

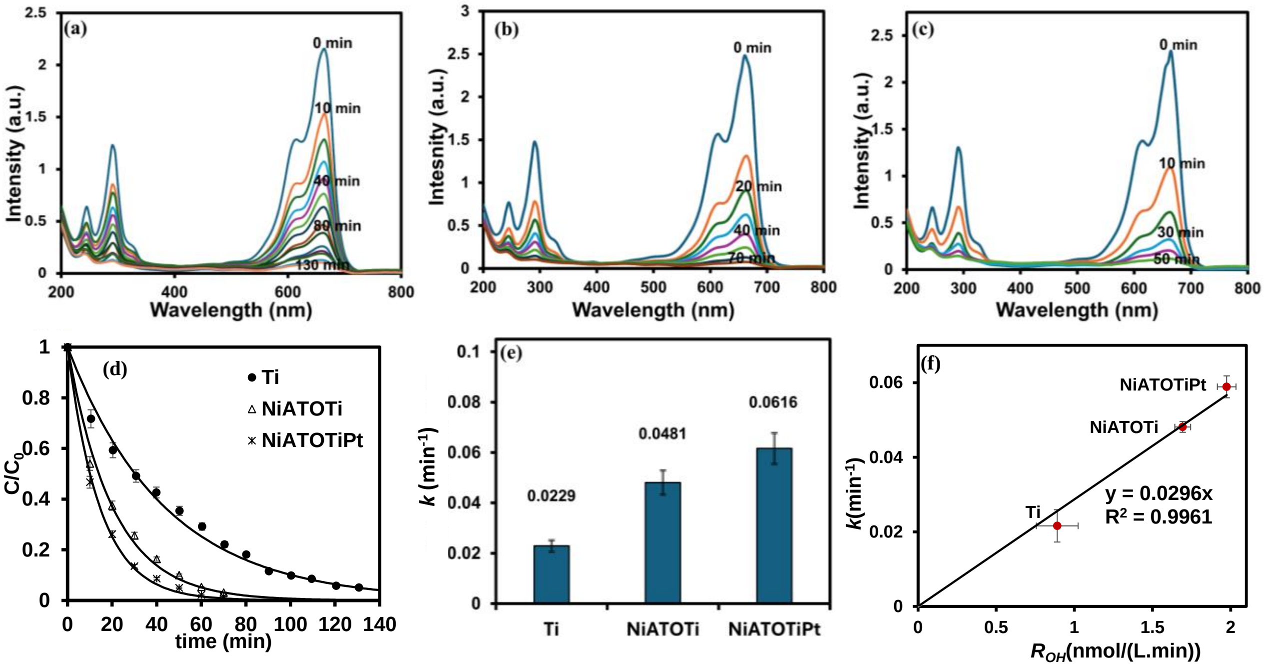

Fig. 8: UV/Vis spectra of MB degradation using the three electrodes (a) Ti, (b) NiATOTi, (c) NiATOTiPt; (d) C/C_0 vs time fitting with a pseudo-first-order model; (e) pseudo-first order rate constant; (f) relationship between pseudo-first order rate constant, *k*, and hydroxyl radical generation rate (R_{OH}) (C_0 = 10 mg/L, Voltage = 5 V, flow rate= 88.5 mL/min).

Figure9

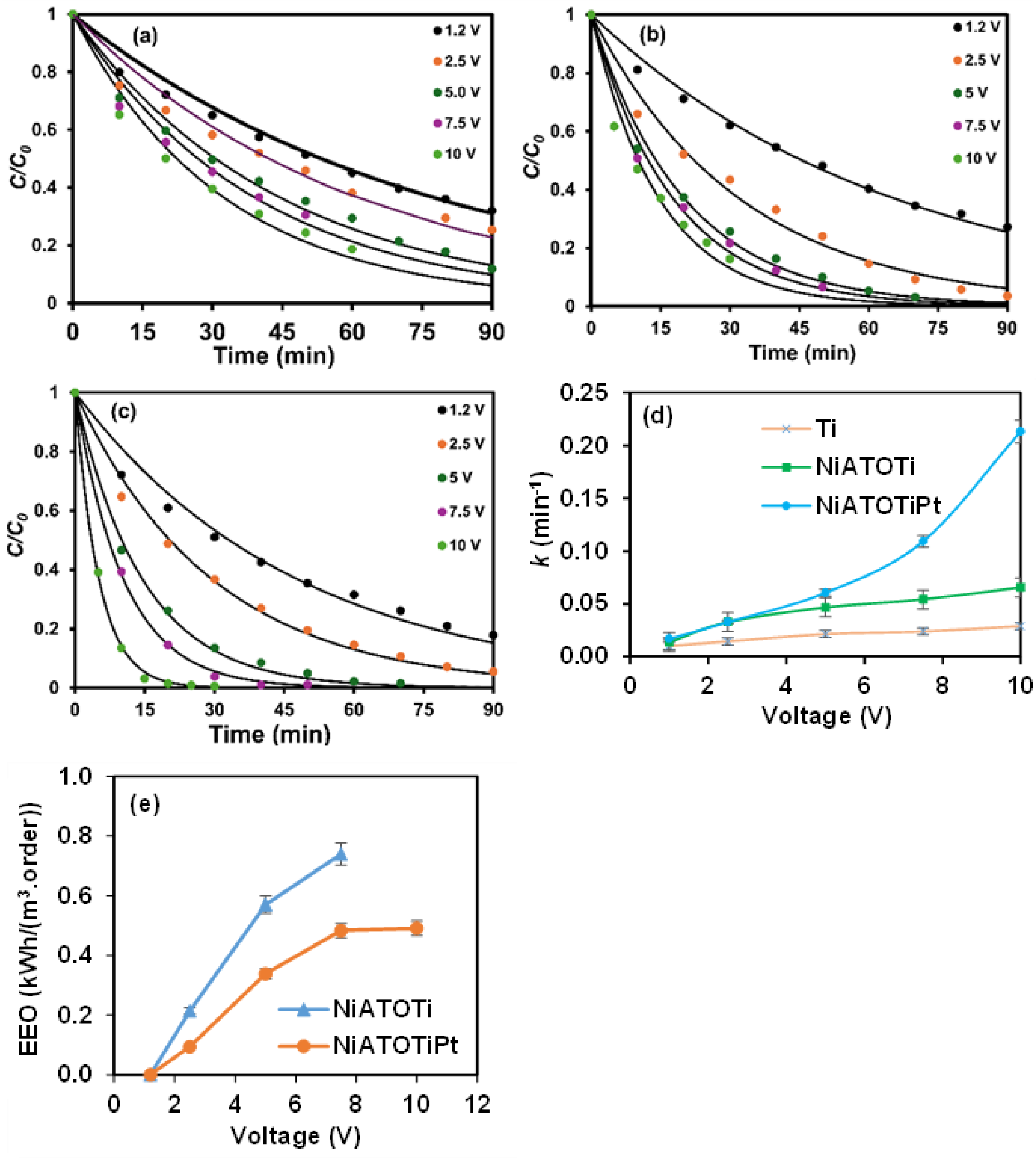

Fig. 9: Effect of voltage on MB degradation using (a) Ti (b) NiATOTi (c) NiATOTiPt electrodes; (d) effect of voltage on pseudo-first-order rate constants; (e) effect of voltage on Electrical Energy per Order (C_0 = 10 mg/L, flow rate = 88.5 mL/min)

Figure10

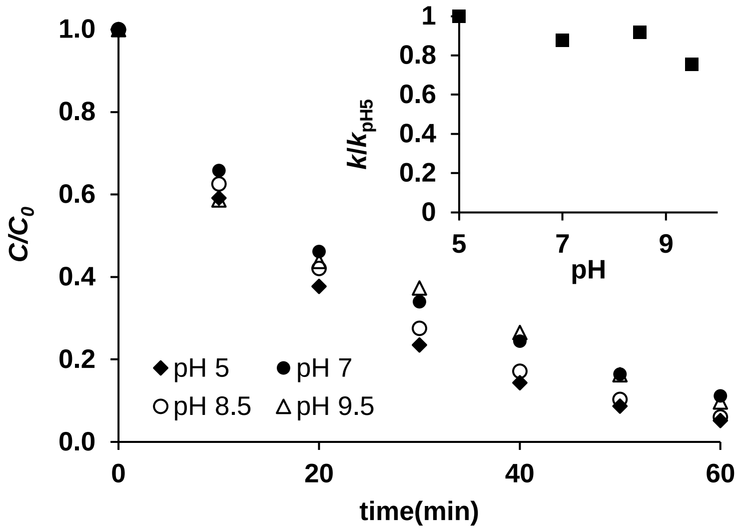

Fig. 10: Effect of pH on the performance of NiATOTiPt (C_0 = 10 mg/L, flow rate = 88.5 mL/min, V = 5V).

Figure11

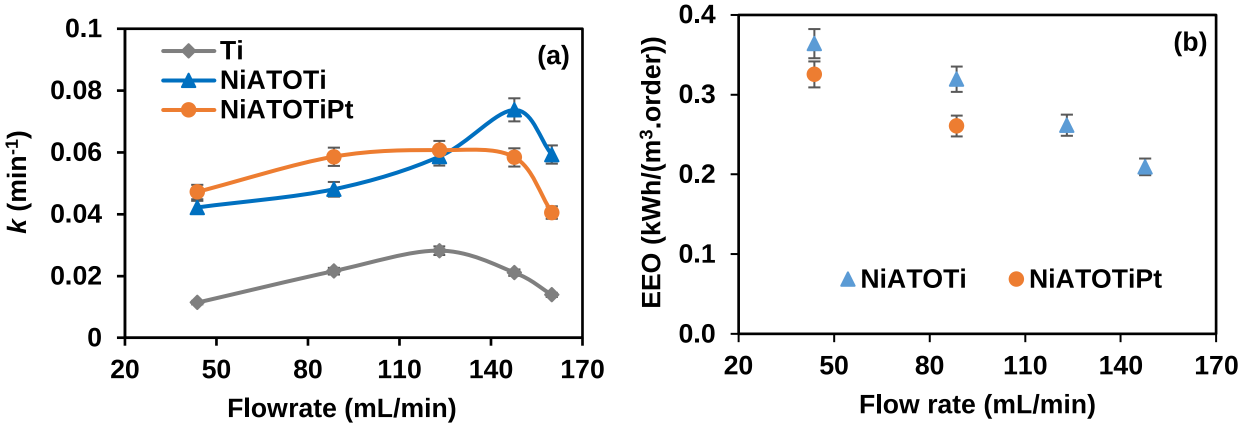

Fig. 11: Effect of circulation flow rate on (a) pseudo-first-order rate constants and (b) Electrical Energy per Order - flows causing channeling are excluded (C_0 = 10 mg/L, voltage = 5 V)

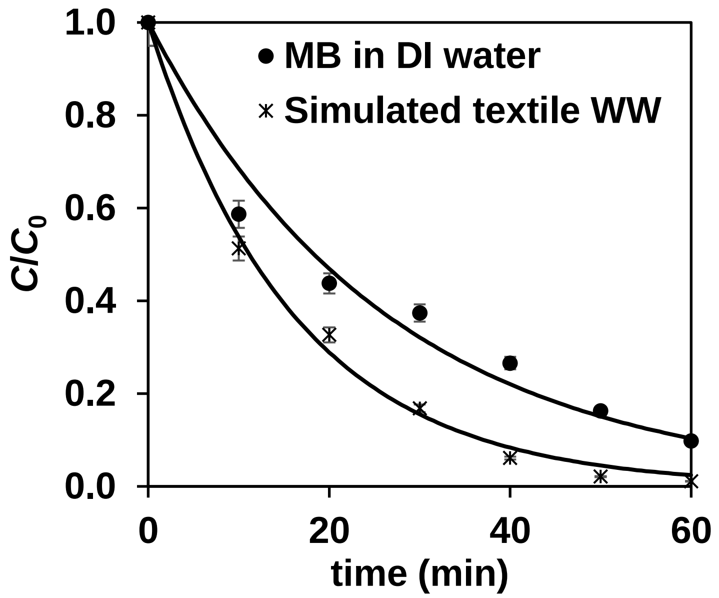

Fig. 12: Effect of water matrix on temporal variation of dye concentration ratio (C/C_0) (electrode = NiATOTiPt, C_0 = 10 mg/L, flow rate = 88.5 mL/min, V = 5V).

Figure13

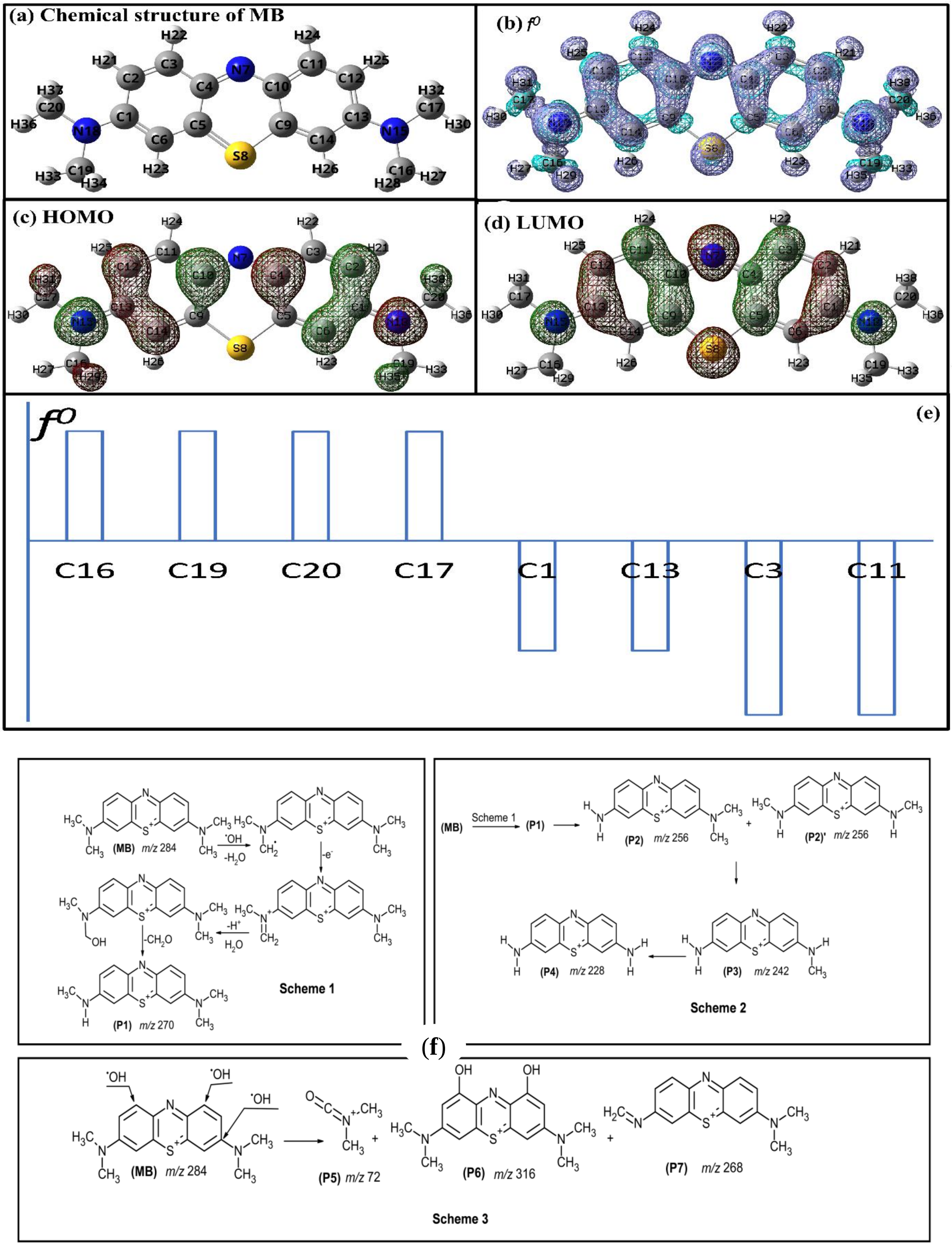
(a) Chemical structure of MB
(b) f^0
(c) HOMO
(d) LUMO
f^0
(e)
C16
C19
C20
C17
C1
C13
C3
C11
(f)
(MB) m/z 284
•OH
-H2O
-e-
-H+
H2O
-CH2O
(P1) m/z 270
Scheme 1
Scheme 1
(P2) m/z 256
(P2)' m/z 256
(P3) m/z 242
(P4) m/z 228
Scheme 2
(P5) m/z 72
(P6) m/z 316
(P7) m/z 268
Scheme 3

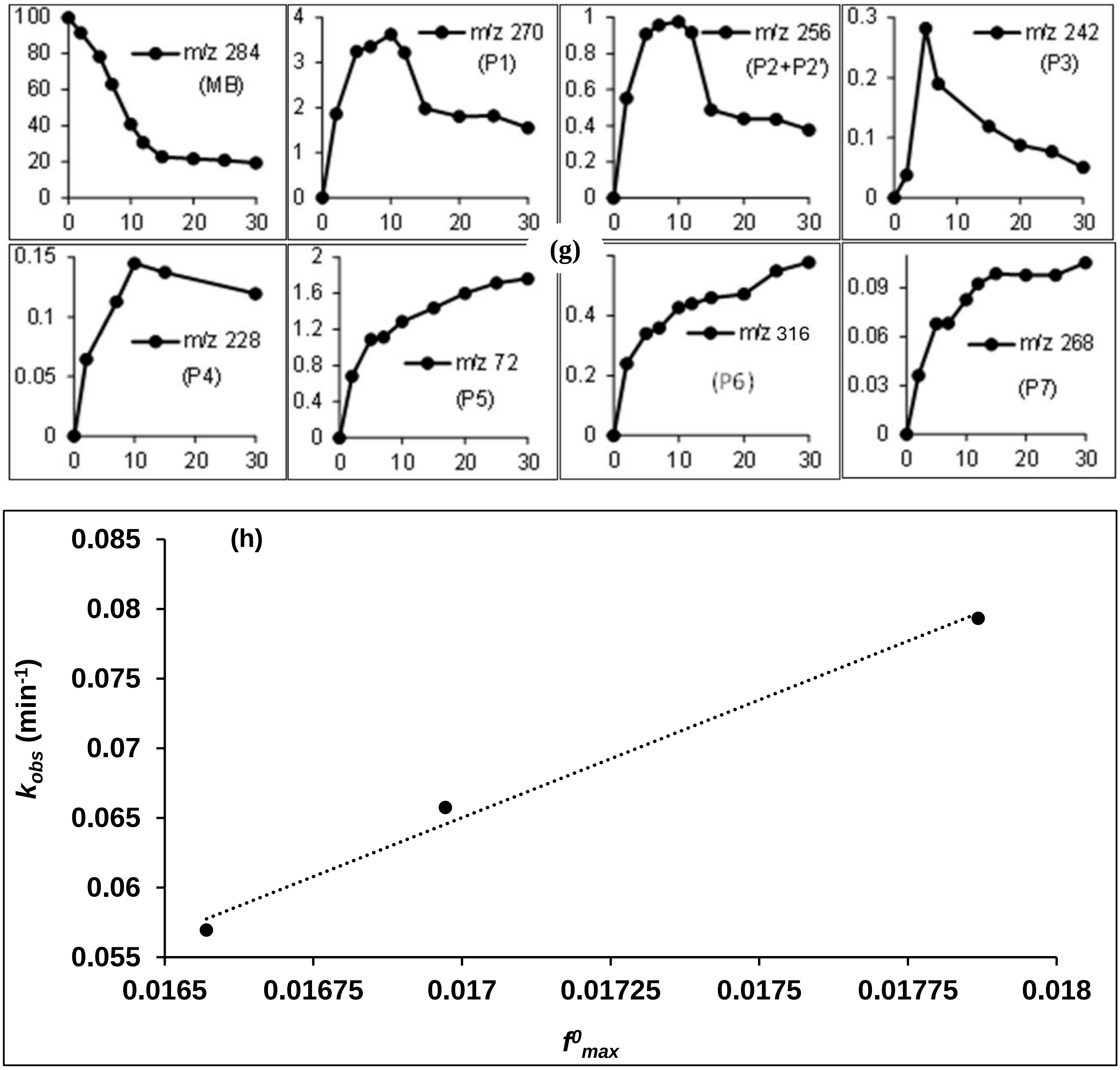

Fig. 13: (a) Chemical structure of MB; (b) Fukui function, f^0, map; (c, d) HOMO and LUMO orbitals of MB; (e) largest first 8 f^0 indices for MB**;** (f) possible mechanism of N-demethylation and degradation pathways of MB by NiATOTiPt electrode; (g) change of products' relative abundance versus time (C_0 = 100 µg/L; voltage = 10 V, circulation flow rate = 89 mL/min, NiATOTiPt electrode) [**x-axis**: time in minutes; **y-axis**: peak area of the corresponding *m/z* ratio to the peak area of MB at t = 0 min]; (h) structure-activity relationship between first-order-rate constant and maximum radical susceptibility Fukui index (f^0_{max}).